

A Global Dilepton Analysis in the $e\mu$ Channel

Ariana Sage Minot

Department of Physics,
Duke University

Spring 2010

Thesis Committee:

Professor Mark Kruse, Ph. D (Advisor)

Professor Seog Oh, Ph. D

Professor Kate Scholberg, Ph. D

Professor Stephen Teitsworth, Ph. D

Abstract

In this study, we conduct preliminary steps necessary for developing an analysis of dilepton events in the first ATLAS collision data. Using ATLAS Monte Carlo samples at $\sqrt{s} = 10$ TeV, we study the contributions of various Standard Model processes to the high- p_T dilepton sample consisting of an electron and a muon of opposite charge. Our three main signal processes are $t\bar{t}$, WW , and $Z \rightarrow \tau\tau$. The background processes that we examine are $W + \text{jets}$ where a jets fakes a lepton, $W + \gamma$ where the γ fakes an electron, WZ , and ZZ . The $e\mu$ events from each sample are plotted in the phase space of number of jets, N_{jets} , versus missing transverse energy, \cancel{E}_T , which provides a nice separation between the signal processes. For an event that lands at a given coordinate in the (N_{jets}, \cancel{E}_T) phase space, we estimate the probability that it came from a given process using the expected 2-D distributions of the processes considered. All findings are consistent with our qualitative expectations based upon the theoretical cross-sections for the different processes at ATLAS at $\sqrt{s} = 10$ TeV. This analysis will be used to monitor the first $e\mu$ events that are recorded by ATLAS as a means to evaluate their consistency with the Standard Model. Additionally, in an independent study, we assess the possibility of measuring the mean interaction length in the ATLAS Transition Radiation Tracker straws by examining a correlation found in both cosmic data and ATLAS Monte Carlo. While we conclude that this parameter cannot be determined using this method, the study nonetheless helps towards furthering our understanding of charge collection in the TRT.

Acknowledgements

First, I would like to thank my advisor Mark Kruse for all of his help and support these past two years. Most of all, I appreciate that he always made an effort to ensure that I not lose sight of the physics behind my research when it was easy to get caught up in the details of computer programming. I would also like to thank the other members of the Duke ATLAS Group for sponsoring my summer at CERN and to Ayana Arce and Esben Klinkby for their help in this analysis.

I also owe a large thanks to the Duke Neutrino Group for their guidance and helping me develop as a scientist during my first research experience. Thank you to all of my professors these past few years. I appreciate especially all of your time during office hours and outside the classroom which has been invaluable to me. I would also like to thank the Duke Physics Department. Being a part of this community has been a lot of fun and very positively shaped my Duke experience.

Finally, I would like to thank my family and friends for always being there and helping me keep things in perspective.

1 Introduction to the Standard Model

The Standard Model is the theoretical framework that best describes our understanding of all known elementary particles and their interactions. It came into being in the mid 1970's, although several of the theories upon which it is based date much earlier.

1.1 Elementary Particles of the Standard Model

The question of what makes up matter at the most fundamental level has been central to the development of particle physics. The Standard Model provides what many physicists consider the best, if incomplete, answer to this question.

The Standard Model contains several kinds of elementary particles that are categorized into families. There are various levels of distinction between these families and a hierarchy that emerges. First, all known elementary particles are either fermions or bosons. Fermions are what one would think of as comprising ordinary matter. They have odd integer half spins and are organized in two families, leptons and quarks. The lepton family consists of six elementary particles, excluding the corresponding antiparticles, see Table 1. The lightest and first discovered is the electron, e . The μ and τ particles were subsequently discovered much later. These three particles are listed in order of increasing mass and all have unit charge. In addition, each of these leptons has a corresponding neutrino (ν_e, ν_μ, ν_τ), which is electrically neutral. Neutrinos are only weakly interacting, whereas the electron, muon, and tau are both weakly and electromagnetically interacting [1].

Particle Name	Charge	Mass (MeV)
e	-1	$0.510998910 \pm 1.3 \cdot 10^{-8}$
ν_e	0	$< 2 \cdot 10^{-6}$
μ	-1	$105.658367 \pm 4 \cdot 10^{-6}$
ν_μ	0	< 0.19
τ	-1	1776.84 ± 0.17
ν_τ	0	< 18.2

Table 1: Properties of leptons

	Flavor	Charge	Mass
First Generation	u	+2/3	1.5 to 3.3 MeV
	d	-1/3	3.5 to 6.0 MeV
Second Generation	c	+2/3	$1.27_{-0.11}^{0.07}$ GeV
	s	-1/3	105_{-35}^{25} MeV
Third Generation	t	+2/3	$4.20_{-0.07}^{0.17}$ GeV
	b	-1/3	$171.3 \pm 1.1 \pm 1.2$ GeV

Table 2: Properties of quarks

Quarks, the other family of fermions, are also strongly interacting and come in six different types. Like the lepton family, quarks come in three different generations of increasing mass, see Table 2. The three quarks with electric charge $2/3$ are, in order of increasing mass, the up, charm, and top quark, and the three quarks with electric charge $-1/3$ are, in order of increasing mass, the down, strange, and bottom quark. In addition to electric charge, quarks also possess a property called color charge, which is either red, blue, or green and which is the charge on which the strong force acts. Of note, quarks do not appear alone in nature, but in hadrons, which are composite particles made of quarks. In addition, all known hadrons that occur in nature have the property of being colorless. Hadrons that are composed of two quarks, a quark and an anti-quark, are called mesons, whereas hadrons composed of three quarks or anti-quarks are named baryons. Up and down quarks comprise protons and neutrons, and the heavier generations of quarks have been detected in cosmic rays or produced in accelerators. The various types of quarks are summarized in Table 2.

Particle	Interaction Mediated	Charge	Mass
γ	Electromagnetic	0	0
g	Strong	0	0
W^\pm	Weak	± 1	80.403 ± 0.029 GeV
Z^0	Weak	0	91.1876 ± 0.0021 GeV

Table 3: Properties of known gauge bosons

In addition to classifying the fundamental constituents of matter, the Standard Model, also describes the electromagnetic, weak, and strong interactions between matter. According to the Standard Model, fermions interact through the exchange of a gauge boson. Distinct from fermions, bosons are force mediators and have integer spin, namely 1 for the cases of the electromagnetic, weak and strong interactions, listed in Table 3. The most familiar is the photon, a massless particle which mediates the electromagnetic force. The W^\pm and Z^0 , bosons are force carriers for the weak force, and the gluon, of which there are eight kinds, mediates the strong force between quarks.

In summary, the Standard Model categorizes the known elementary particles into families, as well as predicts the existence of an as yet undiscovered particle, the Higgs boson. Experimental

discoveries in high-energy physics throughout the twentieth century have consistently confirmed predictions of the Standard Model, demonstrating its success in describing nature. However, the Standard Model cannot be a complete theory as it does not provide explanations for several observations, for example, the presence of dark matter and dark energy, and the incorporation of the gravitational force.

2 The Large Hadron Collider(LHC) at CERN

The Large Hadron Collider (LHC) is a 27 km circumference circular accelerator located at the European Center for Nuclear Research (CERN). CERN straddles the French-Swiss border near Geneva, Switzerland, and the LHC is situated underground at this site. The LHC is the largest, most powerful particle accelerator ever built and has been designed to produce 14 TeV center-of-mass energy proton-proton collisions. The rate of these collision events is about a billion per second. At this energy, the LHC will provide experimental evidence of the Higgs boson if it exists. The Higgs boson is predicted by the Standard Model to be the mechanism which endows mass upon elementary particles. In addition to testing this unconfirmed feature of the Standard Model, it is hoped that the LHC will also shed light on physics that cannot be explained by the Standard Model.

Before they enter the LHC, a series of older accelerators bring the energy of the protons up to 450 GeV. First, the protons for the collisions are obtained by stripping the electrons off of hydrogen atoms. These protons are then injected from the linear accelerator (LINAC2) into the PS Booster, to then be accelerated in the Proton Synchrotron (PS), after which they travel around the Super Proton Synchrotron, and finally enter the LHC. This process is schematically represented in Figure 1.

CERN Accelerator Complex

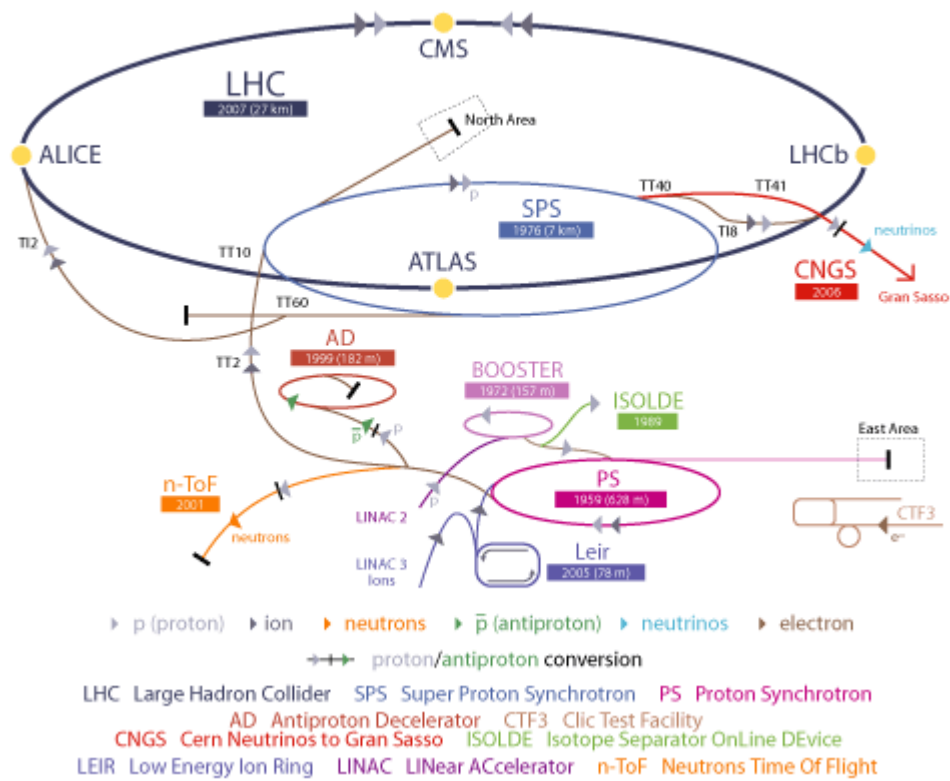


Figure 1: LHC Accelerator Complex, taken from CERN LHC accelerator complex website [2].

After passing through these initial stages, bunches of protons are accelerated in clockwise and counter-clockwise directions. The LHC is a highly sophisticated synchrotron which accelerates the protons up to 7 TeV, allowing for 14 TeV center-of-mass energy collisions. The protons maintain their circular orbit through the use of more than one thousand electromagnets. Specifically, 1,232 dipole magnets, which are 15 m in length, bend the beams, and 392 quadrupole magnets, which are 5-7 m in length, are used to focus the beams [2]. The amount of energy the protons can attain is dependent upon the strength of the magnetic fields and their capability to bend the protons paths around the LHC ring. Such high energies are attainable due to the use of super-conducting material. Superconductivity is a property that some materials exhibit at low temperatures. A distribution system of liquid helium cools the magnets to the extremely low temperature of about 2 K or -271° C. Sufficiently cooled superconductive materials allow current to pass with no electrical resistance. The world’s most powerful accelerator prior to the LHC was the Tevatron at Fermilab, which collides protons with anti-protons at a center-of-mass energy on the order of 2 TeV.

3 The ATLAS Detector

The ATLAS detector is built around one collision point of the LHC. ATLAS, A Toroidal LHC ApparatuS, is a general, all-purpose detector used to study the proton-proton collisions. The ATLAS detector is 46 m long, 25 m high, and 25 m wide, making it the largest particle detector ever built. Its weight is roughly 7000 tonnes [4]. Composed of a series of concentric cylindrical subdetectors, these components work together along with the end-cap detectors to measure the energy and momentum of the various decay products resulting from the collisions. Additionally, each component has been built to identify different properties, which allows the ATLAS detector to distinguish between different particle types. This utility is demonstrated in Figure 2, and a schematic of the entire ATLAS detector is shown in Figure 5.

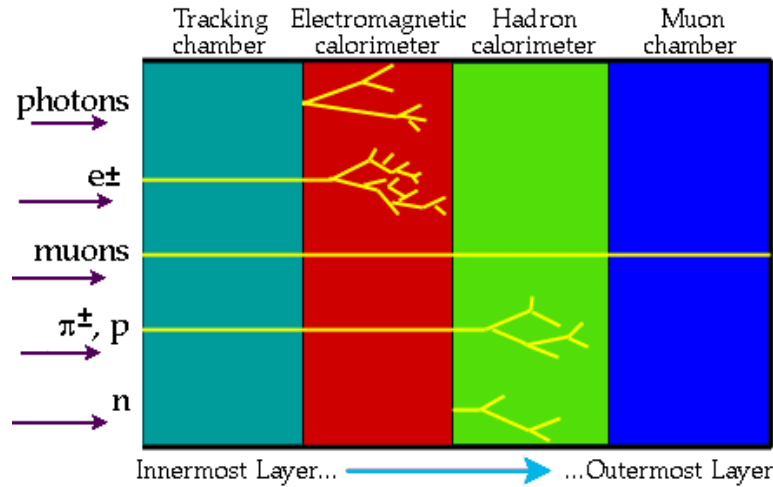


Figure 2: Schematic of How Detector Components Identify Different Particle Types, taken from ATLAS Experiment e-Tour [4].

All particles resulting from the collision will pass through the detector components sequentially. The left-side of Figure 2 represents the innermost cylindrical layer of ATLAS, while the left-most side of Figure 2 depicts the outermost layer of ATLAS. In addition to these concentric cylindrical components which form the “barrel” of the ATLAS detector, there are also two end-caps on either side of ATLAS which contain further detection equipment. Charged particles are detected in both the tracking chambers of the inner detector and the electromagnetic calorimeter. Neutral particles are distinguished from charged particles since they can leave a signal in outer layers of the detector without leaving a trace in the tracking chamber. As shown in Figure 2, different particles leave unique signatures in the detector. For example, a proton is identified by selecting tracks which are matched to energy detected in the hadronic calorimeter. However, it is important to note that particles can fake the signal of another particle through certain background events. Thus, if a particle is detected as only having left a signal in the electromagnetic calorimeter with no associated

track, we can only be fairly certain rather than sure that it is a photon. The cylindrical detector components are built around the beam pipe and centered about the collision point. In the ATLAS coordinate system, the z -axis runs along the beam line.

3.1 Inner Detector

The inner detector contains three main components: the Pixel Detector, Semiconductor Tracker (SCT), and Transition Radiation Tracker (TRT), as shown in Figure 3. These three subdetectors are subject to a solenoidal field of nominal value 2 T [4]. The solenoidal field is created by winding wires cylindrically to produce a straight uniform field within the coil. The magnetic field, along with certain silicon technologies, is used in these tracking systems. With the knowledge of certain physical principles, a particle's charge and momentum can be measured. The path of a charged particle curves in the presence of an external field. Oppositely charged particles will bend in opposite directions in the presence of a magnetic field, whereas the trajectory of neutral particles will not be curved by the magnetic field. Furthermore, since neutral particles do not ionize they will not leave an actual track in the Inner Detector but instead deposit all their energy in the Hadronic Calorimeter. Additionally, the degree to which a charged particle's path is curved by the magnetic field serves as a measure of its momentum. Since a particle with higher momentum will travel more quickly through the field, its trajectory will be relatively less curved by the field than that of a similar particle with a lesser momentum.

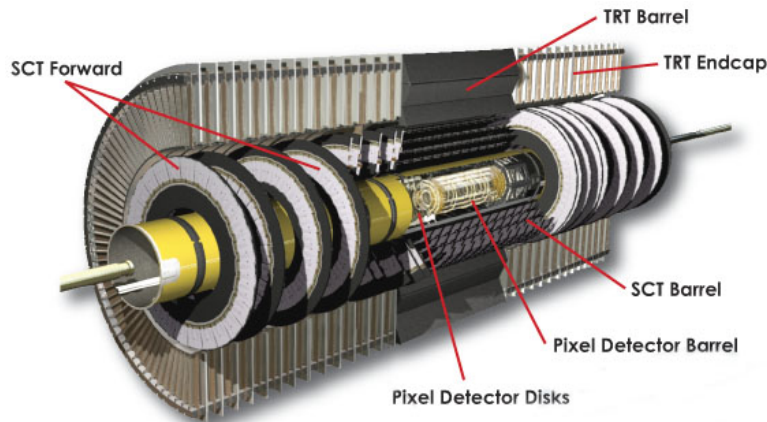


Figure 3: ATLAS Inner Detector Diagram, taken from ATLAS Experiment e-Tour [4].

3.1.1 Pixel Detector

The Pixel Detector is located closest to the collision point and provides a high precision and high granularity set of position measurements. The individual pixel sensors are made up of thin layers

of silicon which are subdivided into rectangular regions, called pixels and have dimensions of 50 by 300 microns [4]. When a charged particles passes through these pixel devices, an electronic signal is produced identifying which pixel has been traversed and thus providing tracking information. This position measurement is precise enough to determine if the particle came from the proton-proton collision point or if the particle is a decay product that originated a few millimeters from the collision point. Additionally, the Pixel Detector is used to determine impact parameter and to detect very short-lived particles. In order to achieve such precision, the Pixel Detector is composed of three cylindrical concentric layers along the beam axis of radii roughly 5 cm, 9 cm, and 12 cm, as well as three disks perpendicular to the beam axis on either side having radii between 9 and 15 cm. On average, three layers are crossed per particle track [4].

3.1.2 Semiconductor Tracker (SCT)

The Semiconductor Tracker provides additional position measurements that combined with information from the Pixel Detector more fully determine particles' trajectories. Similar to the Pixel Detector, the SCT has layers arranged parallel to the beam axis around the barrel of the ATLAS detector and layers arranged radially around the end-caps of the ATLAS detector. The SCT is composed of eight layers of silicon microstrip detectors, and each layer consists of two strips which lay at a small angle with respect to each other. The individual microstrip detectors are about 80 microns wide and several centimeters in length [4]. Like in the pixel detectors, when a particle traverses a strip detector, an electrical signal is produced. Finally, although pixel detectors provide more tracking information, it would be too expensive to use them solely throughout the inner detector.

3.1.3 Transition Radiation Tracker (TRT)

The TRT is made up of a series of gas-wire drift detectors shaped like straws. These straw detectors are 4 mm diameter metal tubes filled with a Xe-gas based mixture, and each has a thin wire running along its center. A high-voltage is kept between the wall of the straw tube and the central wire. As a charged particle passes through a tube, it ionizes the surrounding gas and thus produces primary electrons (PE), see Figure 4. Due to the potential difference, these primary electrons travel to the wire at the center of the straw, which then causes an avalanche of electrons close to the wire giving rise to a detectable electrical signal that is sent to the end of the straw. For each straw, only the leading and trailing edge times are recorded, see Figure 9. The leading edge time is the time it takes the PE produced closest to the wire to reach the wire, and the trailing edge time is the equivalent time for the PE produced furthest from the wire. In addition to the position measurements based upon which straws are hit, the TRT also has the capability through accurate timing measurements to determine the particle's distance from the wire.

Furthermore, the TRT is also used to identify electrons by detecting transition radiation. Charged particles that travel near the speed of light and cross boundaries of materials with different

dielectric constants, here implemented by using a radiator “foam” that surrounds the straws, generate X-rays, called transition radiation. These X-rays can pair produce near the straw to give rise to an additional signal, see Figure 4. The transition radiation produces a much larger signal than the other passing charged particles. Since electrons have a relatively low rest mass compared to other charged particles, only their velocities at LHC energies can be high enough to produce transition radiation. Thus when such large pulses are identified, this serves as a means of identifying electrons. The straws are a maximum length of 144 cm in the barrel, which holds about 50,000 straws. The barrel straws run parallel to the beam axis, and each is divided in two at the center and read out at either end. The end-caps contain 320,000 radial straws with each readout at the outer radius of the straw [4]. In conclusion, the TRT provides tracking information for ATLAS radii between 50 to 100 cm and has the capability to identify electrons.

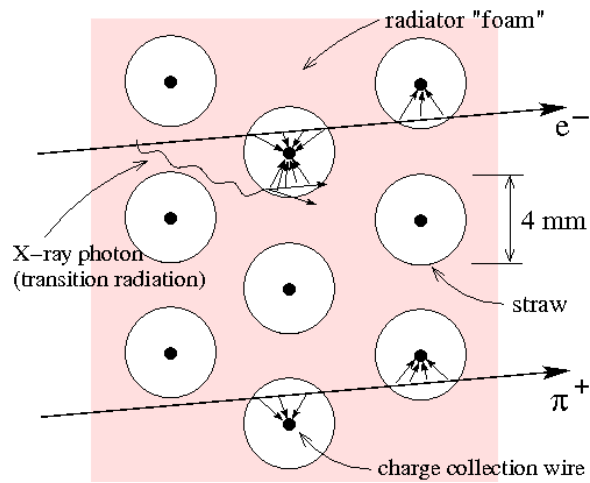


Figure 4: Processes that occur as a particle traverses a TRT straw, created by Dr. Mark Kruse.

3.2 The Calorimeters

The ATLAS calorimeters surround the inner detector and measure the energy of the particles resulting from the proton-proton collisions. Their position within the ATLAS detector is shown in Figure 5.

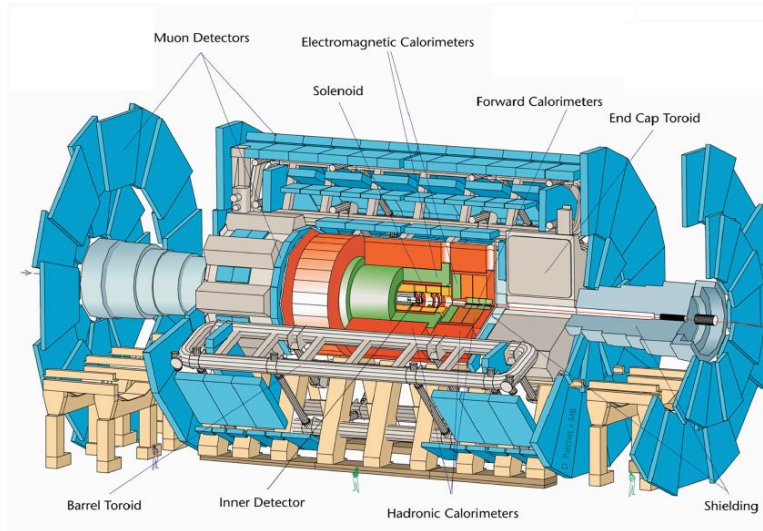


Figure 5: ATLAS Calorimetry and Muon Detector Diagram, taken from CERN visits website [3].

The calorimeters have two basic components: metal absorbing plates and sensing elements. As collision products interact with the metal absorbing plates, their energy is transformed into a shower of particles, which are then detected by the sensing elements.

3.2.1 The Electromagnetic (EM) Calorimeter

The electromagnetic calorimeter measures the energies of electrons and photons passing through the ATLAS detector. The EM calorimeter is made up of 1.5 mm thick lead plates, and as photons and electrons of high enough energies pass through these lead plates, an electromagnetic shower is produced. The high-energy electrons radiate electromagnetic energy in the form of gamma-ray photons as they are deflected from the electric fields associated with the lead nuclei. As for the high-energy photons, in the presence of lead nuclei, they can transform into electron-positron pairs. Then, this electron and positron will in turn radiate photons, which contribute to the electron-positron pair production. Since this effect falls off quickly with increasing mass, at LHC energies, only electrons will be able to exhibit such behavior due to their relative lightness. The magnitude of the electron shower is proportional to the energy of the incident electron or photon, and it is the magnitude of the electron shower which is measured by the calorimeter.

The lead plates are immersed in liquid argon, which has several properties that make it a very suitable sensing material. The shower electrons produced in the lead will leave the lead plates and travel in the liquid argon. As they pass through this material, they will ionize the surrounding argon atoms, leaving behind a path of electron-ion pairs. The liquid argon is subject to an electric field, which causes the ionization electrons to separate from their ion partner and travel to the positively charged plates. The motion of these electrons produces an electrical current, which is measured.

The magnitude of this current is proportional to the incident energy.

The EM calorimeter also aids in determining the direction in which energy is being deposited since the readout structure of the calorimeter has been segmented in order that current signals can be associated to different positions within the detector. Regions of the detector are described in terms of pseudorapidity, η , which is a function of the angle of a particle's momentum relative to the beam axis, θ . Pseudorapidity is defined as $\eta = -\ln[\tan(0.5\theta)]$. For example, the forward regions of ATLAS are those at a small angle with respect to the beam axis and of high values of η . Although the angular width of different $|\eta|$ regions is not equal, pseudorapidity is a useful quantity since it produces Lorentz invariance along the beam axis. Roughly speaking, we expect about equal numbers of particles to be produced per unit of pseudorapidity. Lead plates and liquid argon are used in both the barrel region, corresponding to $|\eta| < 1.4$, and in the end-cap region, $1.4 < |\eta| < 3.2$, of the EM calorimeter [3].

3.2.2 The Hadronic Calorimeter

The hadronic calorimeter surrounds the electromagnetic calorimeter, and its purpose is to measure the energies of hadrons, such as protons and neutrons. Although hadrons do deposit energy in the electromagnetic calorimeter, they will be energetic enough to continue past this region of ATLAS and into the hadronic calorimeter, which will fully determine their energies. Electrons and photons will have been stopped before reaching the hadronic calorimeter. A hadronic shower spans tens of centimeters typically, whereas an electromagnetic shower's length is on the order of only a few centimeters [4]. Therefore, the hadronic calorimeter is required to be much thicker than the electromagnetic calorimeter.

Unlike the EM calorimeter, the technology used in the hadronic calorimeter varies between the barrel and end-caps. The layout of the hadronic calorimeter is shown in Figure 6.

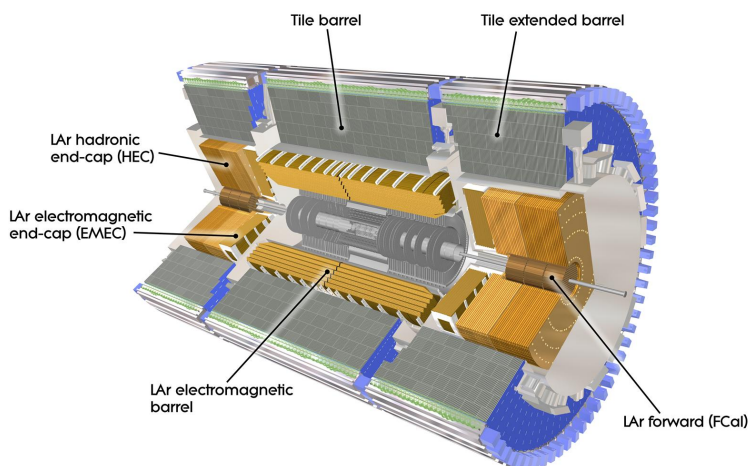


Figure 6: ATLAS Hadronic Calorimetry , taken from CERN Media archive website [3]

In the barrel portion, there is a tile calorimeter composed of steel absorbers and tiles of scintillating plastic used as sensing material. As a high-energy hadron traverses the metal plates, it will interact via the strong force with the steel nuclei and produce a hadronic shower, mostly pions and sometimes kaons. Some of the hadron's incident energy will be transformed into the rest mass of these new hadrons, and some of its' energy will go into the kinetic energy of these newly created hadrons. Furthermore, a portion of the incident hadron's energy is lost to disrupting the steel target nucleus, knocking off some of their protons and neutrons. If the created hadrons have enough energy, they in turn will produce more showers and disrupt other steel nuclei. Both the disrupted nucleons from the steel and the primary and secondary hadronic shower particles contribute to the signal produced in the scintillator, which is proportional to the incident energy.

Due to quantum chromodynamic confinement, quarks and gluons produced in the proton-proton collisions will draw quark-antiquark pairs or gluon-antigluon pairs from the quantochromodynamic vacuum in a process known as hadronization. Therefore, the hadrons that enter the calorimeter are often part of a cluster of many other hadrons. The energy of the hadron jet, rather than of the individual hadrons, is the quantity of most interest since it represents the energy of the original quark or gluon. The hadronic calorimeter is responsible for helping to determine the energy of jets.

In addition, the total energy in the transverse plane is measured to determine the presence of neutrino particles. Neutrino particles are only weakly interacting and leave no detectable signature in the detector, so their presence must be inferred indirectly. This is accomplished by utilizing the principle of conservation of momentum. The total momenta of the collision products must vector sum to zero since the incident momenta of the two protons is equal and opposite. We do not know the initial momenta of the individual partons that make up the colliding protons, so we can only verify that momentum in the transverse plane is conserved. If the transverse components

of momentum add up to a nonzero result, then this missing transverse energy, \cancel{E}_T , indicates the presence of neutrinos among the decay products.

The regions of ATLAS that are at a small angle with respect to the beam-line receive most of the radiation from the collisions, and therefore the end-caps and forward region of the hadronic calorimeters use devices that are more radiation resistant than the tile calorimetry used in the barrel region. Additionally, these regions require a different design to provide speed of response that will handle the higher flux of particles and energy in this region.

The end-cap hadronic calorimeter uses a liquid argon device similar to that in the EM calorimeter but uses copper instead of lead plates as an absorber since these materials are better suited for measuring hadronic showers. A forward calorimeter is positioned radially closest to the collision point and extends along the beam line with the hadronic end-caps, see Figure 6. This is both one of the most kinematically important as well as irradiated regions of the detector. Liquid argon and copper are also used, but instead of using a plate design, the copper has been formed into a matrix with tubular holes. Metal rods are then inserted into these tubes, leaving a thin gap between the outer diameter of the rod and inner diameter of the tube. A potential difference is kept between these two surfaces, and liquid argon fills this small gap. The use of narrow gaps was chosen to avoid an electrical problem that can occur in high radiation environments when there is a build-up of positive argon ions. The forward liquid argon calorimeter serves to provide full coverage for measuring jets [3].

3.3 The Muon System

The muon system is the outermost layer of ATLAS and provides a more accurate measurement of the momenta of muons. Muons, apart from neutrinos, are guaranteed to be the only particles to enter this part of the detector due to the fact that they deposit much less energy per distance traveled than the other particle types. Muons deposit energy by ionizing the material through which they travel, and the muon system tracks their path by detecting this ionization much like the inner detector. The muon system is divided into three areas, the barrel ($|\eta| < 1.05$), the transition region ($1.05 < |\eta| < 1.4$), and the end-caps ($|\eta| > 1.4$). These regions are depicted in Figure 7. The technologies used in different parts of the muon system were chosen based on several considerations, including count rate, time and space resolution capability, and required radiative resistance [3].

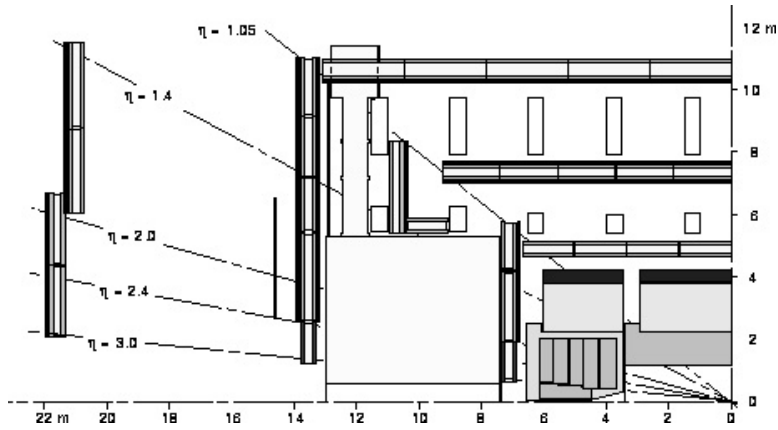


Figure 7: Side view of ATLAS Muon system, taken from CERN Technical Proposal [3].

3.4 The Trigger System and Data Acquisition

Due to the high collision rate, millions per second, a gigantic amount of information will be generated at the LHC. The trigger system is responsible for selecting the most interesting events to be recorded in computers for further processing and eventually analyzed by scientists in the ATLAS collaboration around the world. There are three levels to the ATLAS trigger system, LVL1, LVL2, and LVL3. At LVL1, only data in a reduced form from a subset of detectors is studied. Full-granularity and full-precision data is used at LVL2 from the detectors that LVL1 marked as having interesting information. Finally, at LVL3, the full data from all of ATLAS is used to determine which events will be sent and recorded for analysis.

4 Towards Understanding Charge Collection in the ATLAS TRT from Trailing Edge Information

The effective interaction length in the TRT straws is one of the basic parameters that affects TRT, and ultimately, tracking resolution. The aim of this study is an effort towards determining the effective interaction length and understanding charge collection in the TRT.

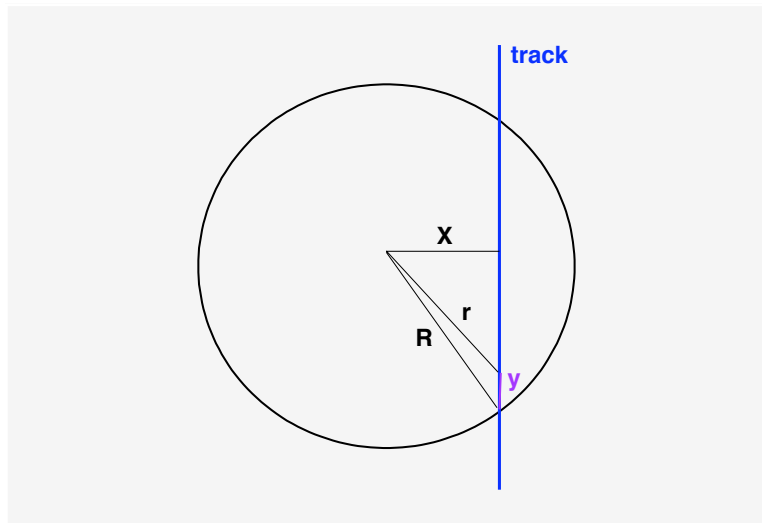


Figure 8: Schematic of TRT straw traversed by a particle track, taken from note by Saša Fratina and Dominick Olivito.

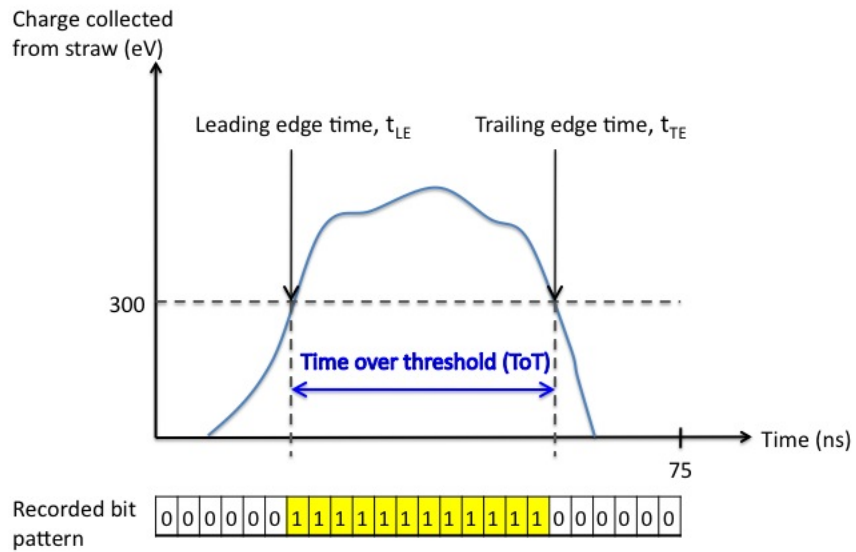


Figure 9: Charge Profile of a TRT Straw, created by Dr. Mark Kruse.

In cosmic data, which consists mostly of muons produced by interactions of cosmic rays with the upper atmosphere, a correlation between two quantities, the impact parameter, X , and the trailing edge time, t_{TE} , is observed. The impact parameter is the distance of closest approach between the central wire of the TRT straw and the reconstructed particle track, see Figure 8. The trailing edge time, is a quantity key to understanding a straw's charge profile for a given event, see Figure 9. A straw's charge profile represents the amount of charge detected at the central wire as a function of time. When the charge at the central wire is above a certain threshold, the bit pattern registers a 1, otherwise a 0 if under threshold. The bit pattern is composed of 24 bits corresponding to 75 ns. When a charged particle traverses a straw, producing primary electrons (PEs) as it travels, some of the PEs are produced closer to the central wire than others, see Figure 4. Since the drift velocity of the PEs in TRT gas is negligible compared to the velocity of the traversing particle (50 microns/ns and 30 cm/ns respectively), one can approximate all PEs to have been produced at the same time. The PEs produced as the particle enters and exits the straw are the furthest away from the wire and thus take the longest to arrive at the central wire. The arrival of these PEs represents the last 1 in the charge profile bit pattern, which defines the trailing edge time, t_{TE} , assuming the PEs produce an avalanche of electrons sufficient to exceed threshold.

At first glance, the dependence of t_{TE} on X is unexpected. If a PE is produced roughly at whatever point the particle enters the straw, it will always travel the same distance to the central wire, the 2 mm radius of the straw, independent of the impact parameter. One proposed explanation for this dependence is that the PE corresponding to t_{TE} is produced at a distance r which is significantly less than 2 mm, thereby reducing t_{TE} . The distance r depends only on X and y , see Figure 8, where y is a function of the mean interaction length. If this is the main physics effect responsible for this dependence, then we can extract the mean interaction length from the given $t_{TE}(X)$ dependency seen in the cosmic data.

To investigate whether or not this is a valid assumption, a toy Monte Carlo(MC) study was conducted to isolate this mechanism. First, a two dimensional histogram of t_{TE} and X was plotted to determine the $t_{TE}(X)$ dependency, see Figure 10. For a given bin of the y -axis, there is a 1-D histogram corresponding to the different values of t_{TE} for all events at that value of X . The contents of this 1-D histogram were fitted to a Gaussian, and the red line with error bars represents the mean and standard error of this Gaussian fit.

The difference between the mean t_{TE} at a given X and the mean t_{TE} at $X=2$ mm defines a relative shift in t_{TE} . This shift as a function of X is shown in Figure 11. In the first column are plots of cosmic data events, and the corresponding plots for full ATLAS MC are in the second column. In the first row, particle tracks with θ between $\pi/6$ and $\pi/3$, where θ is the angle made with the beam axis, are selected. The second row of plots are those for events with θ between $\pi/3$ and $\pi/2$. The y -intercept of the plots in the first row is significantly smaller than for those in the second row, see Figure 11. This is expected since the projection of these tracks in the x - y plane of the straw will place ionization events closer together than they actually are, reducing the mean interaction length. Furthermore, this dependence on θ is observed in both the cosmic data and full MC.

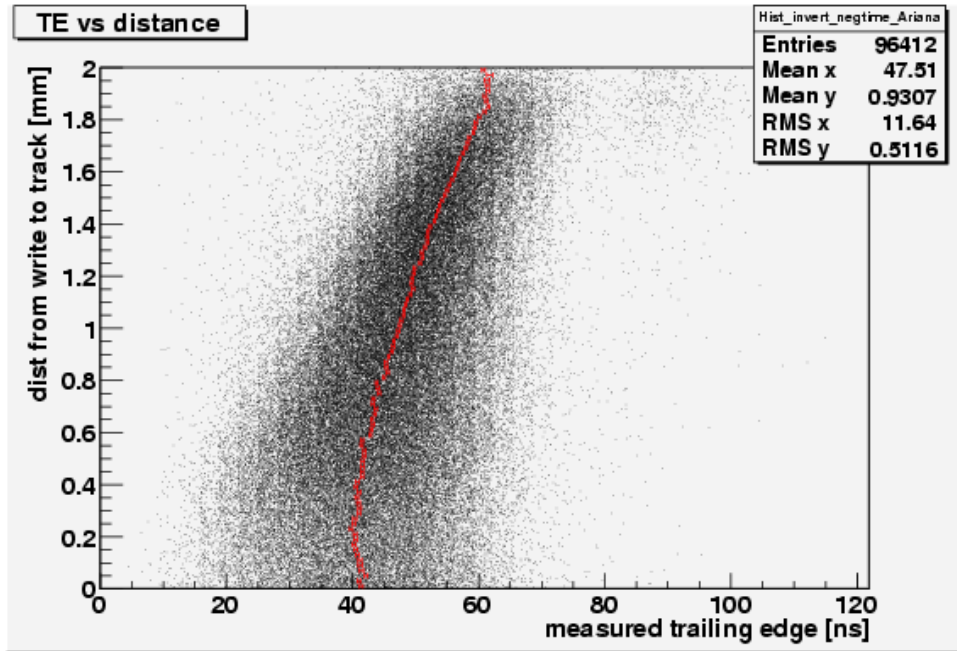


Figure 10: Trailing Edge Time vs. Impact Parameter for Cosmic Data Events.

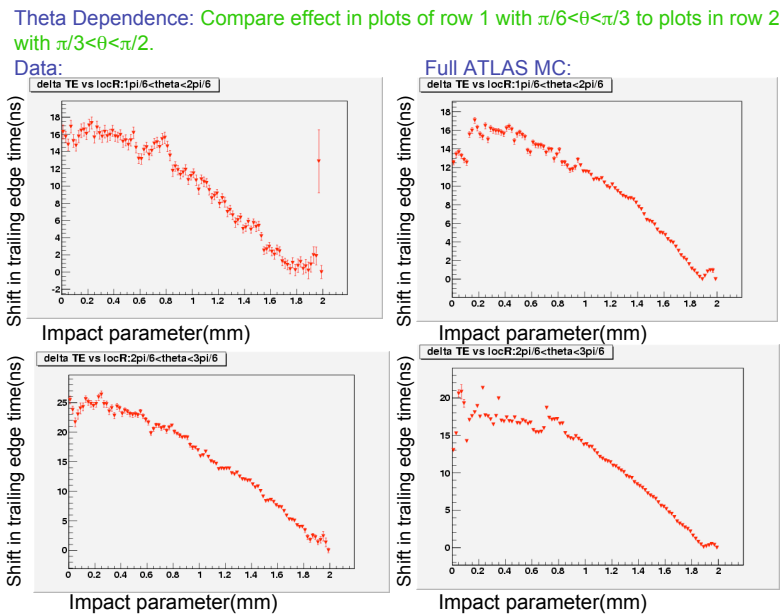


Figure 11: Variation of $t_{TE}(X)$ dependency with θ of particle's track.

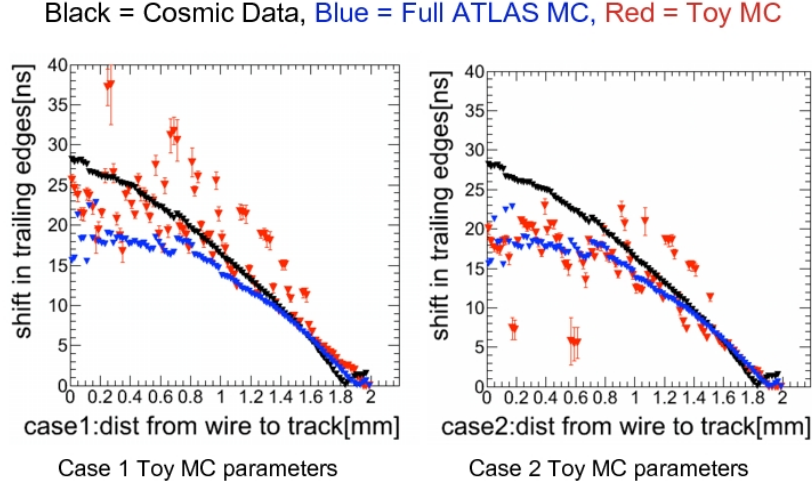


Figure 12: Mean Interaction Length Study Plots

Similar plots were made, for θ between $\pi/3$ and $2\pi/3$, of the cosmic data, full ATLAS MC, and Toy MC events, see Figure 12. These two plots were made with two different sets of Toy MC parameters representing different physical situations that correspond to different values for the effective interaction length. In Case 1, only a few PEs, each with a large amount of energy produce the signal. Whereas in Case 2 similar data is produced but this time many PEs, each with less energy than the PEs in Case 1, arrive at the central wire within a certain time interval. The size of the time interval is chosen to resemble the typical rise time of a signal in the electronics which is about 1 ns [8]. Thus, Case 1 and Case 2 correspond to different values for the interaction length but would reproduce a similar $t_{TE}(X)$ dependency. It is not clear which of the two cases match the data and full MC better as the effect is similarly reproduced in both cases.

In essence, it is very difficult to tell if a signal is due to one high-energy PE or several lower energy PEs that are produced within a certain time interval. This study shows the difficulty in distinguishing between these two cases. The PEs produce an avalanche of electrons that arrive at the wire, and while the size of this avalanche depends on the distribution of the initial energies of the PEs, there is however a large fluctuation in the number of final electrons that one PE gives rise to. Thus from the t_{TE} dependency alone it is not possible to extract the effective interaction length in the TRT. More work will be needed to fully explain this dependence which is observed in both the data and MC in order to better understand ionization in the TRT and the full ATLAS MC simulation.

5 Analysis Strategy for Study of High- p_T $e\mu$ Events

5.1 Standard Model Processes Studied

This analysis serves as the preliminary steps for determining the cross-section of various Standard Model processes which have an oppositely charged electron and muon in the final state from ATLAS data. These processes will be generated by the proton-proton collisions, which can result in quark-quark, gluon-gluon, or quark-gluon collisions. Our signal processes, those producing events with an $e\mu$ dilepton final state, are $t\bar{t}$, WW , and $Z \rightarrow \tau\tau$, (see Feynman diagrams in Figures 13, 14, and 15). The background processes we will be studying are $W + \text{jets}$ where a jet fakes a lepton, $W + \gamma$ where the γ fakes an electron, WZ , and ZZ . The different ATLAS Monte Carlo samples used for these processes are summarized in Table 4. These samples were used to generate ROOT ntuple files by running on the Open Science Grid and using the data structure CuteTuple, a simple ntuple format.

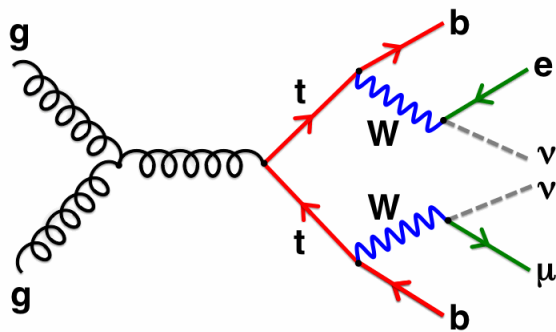


Figure 13: Feynman Diagram for $t\bar{t}$

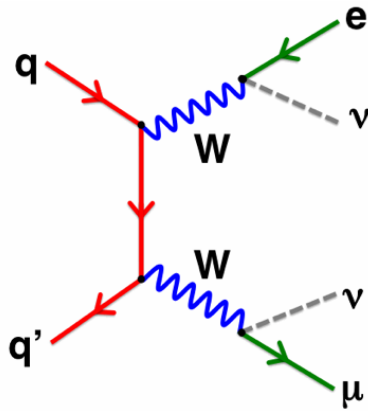


Figure 14: Feynman Diagram for WW

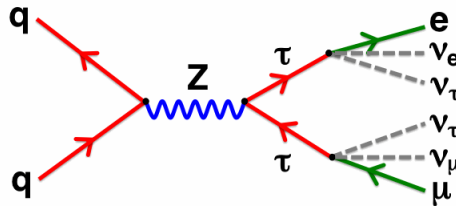


Figure 15: Feynman Diagram for $Z \rightarrow \tau\tau$

Several kinematic quantities and physics objects are key to this analysis, namely electrons, muons, jets, and missing transverse energy, \cancel{E}_T . The transverse momentum, p_T , and the invariant mass of the electron and muon are also studied to better understand the $e\mu$ events.

An $e\mu$ event is selected by choosing events with 1 “good” electron and 1 “good” muon, each with a transverse momentum, $p_T \geq 20$ GeV. Reconstructed values, as opposed to truth information in the MC, are used in identifying the objects and calculating the kinematic quantities relevant to the analysis. Electrons are reconstructed by identifying tracks in the inner detector which extrapolate from the interaction vertex to an energy cluster in the calorimeter that is distinctive to an electron. A series of independent cuts have been developed by the ATLAS team to efficiently identify high p_T electrons and optimized for different η regions of the detector. Three identification categories, loose, medium, and tight, describe increasingly more stringent requirements for identifying an electron.

Thus, the tight electron sample is of lower efficiency than the loose and medium but contains less background contamination. In this analysis, only “good tight” electrons are used. The cuts mainly consist of requirements on shower shape, track isolation, and track to calorimeter cluster matching. The average electron identification efficiency in the barrel is about 75%, whereas in the endcaps, it is roughly 60% [5].

Muon identification and reconstruction relies on extrapolating tracks in the muon spectrometer back to tracks in the inner detector, after taking into account energy loss in the calorimeter. As with electrons, only muons passing certain quality cuts such that they qualify as “good” muons are used in this analysis. All reconstructed muons tracks must have a p_T of at least 5 GeV and be isolated in the inner tracker and calorimeter. Muon detection is possible in the range of $|\eta| < 2.5$, and the average efficiency for detecting a muon is 95% [5].

Jets are reconstructed using the algorithm AntiKT4H1TopoJets. The cone size used in this analysis is 0.4. There is no universal method for identifying jets, but different methods are better suited for certain kinds of analyses. Various subtleties that arise in identifying jets have resulted in the development of different algorithms [6]. All jet identification tools rely on determining the full four-momentum of a jet, and certain guidelines have been agreed upon in the ATLAS collaboration so that a jet is understood to be the same object among different experimenters. The AntiKT4H1TopoJets reconstructs topological cell clusters, a massless pseudoparticle with a certain four-momentum. These can be thought of as 3-D energy blobs that represent showers of particles in the calorimeter. In this particular analysis, all jets are required to have $p_T \geq 20$ GeV, and since jets are often reconstructed as an electron, the $\Delta R = \sqrt{\Delta\phi^2 + \Delta\eta^2}$, between the jet candidate and any electron candidate in the event must be ≥ 0.4 . Otherwise, this jet is discarded.

In addition to identifying electrons, muons, and jets, several kinematic quantities are calculated and plotted to better understand the $e\mu$ events. In particular, those associated with the transverse plane, which is perpendicular to the beam line, are of special interest. Plots of the transverse momentum, p_T , of the leptons and the missing transverse energy, \cancel{E}_T , of the events are shown in Figures 20, 22, and 18. The energy of the electron and muon for $e\mu$ events is plotted in Figures 21 and 23. After calculating the energy in the transverse plane associated with all known objects in the event, the \cancel{E}_T is the energy that cancels such that the total energy in the transverse plane is zero. This is corrected for any muons in the event as muons do not deposit all their energy in the calorimeters, passing through them to leave additional tracks in the outer muon detectors. The reconstructed \cancel{E}_T is a vector object with its magnitude given by the energy and its direction the η and ϕ associated to the cluster that would cancel any transverse energy in the event so that the net transverse energy is zero. Since neutrinos are not directly detectable by ATLAS, most of the \cancel{E}_T is attributed to them and serves as an indirect measure of their presence. To get a sense of how well this quantity is reconstructed, it is noted that the \cancel{E}_T resolution is about 6.5 GeV for diboson events with neutrinos in the final state [5]. The invariant mass of the electron and muon is given by $M_{e\mu} = \sqrt{E^2 - (p_x^2 + p_y^2 + p_z^2)}$, where the energy and momentum of the leptons have been added component-wise. The invariant mass plot is expected to peak at roughly the value of the mass of

the particle from which the electron and muon decayed in the cases where they both came from a decay of a single particle, see Figure 24. Finally, the ϕ and η coordinates of the electrons and muons are shown in Figures 26, 27, 28, 29, where ϕ is the azimuthal angle and η is a function of ϕ .

The three main processes studied ($t\bar{t}$, WW , $Z \rightarrow \tau\tau$) can be well separated by plotting their $e\mu$ events in the phase space of number of jets, N_{jets} , versus \cancel{E}_T in the event, see Figure 19. A schematic of where the 3 signal processes, and some backgrounds, appear in this phase space is given in Figure 16. Ultimately, it is intended to take advantage of this separation in order to extract the SM cross-sections of these main processes. In addition to presenting this phase space for the main processes and several background samples, $e\mu$ events from a top mixed sample, which contains a mixture of MC events of different processes in proportions meant to imitate data, are also plotted in this phase space.

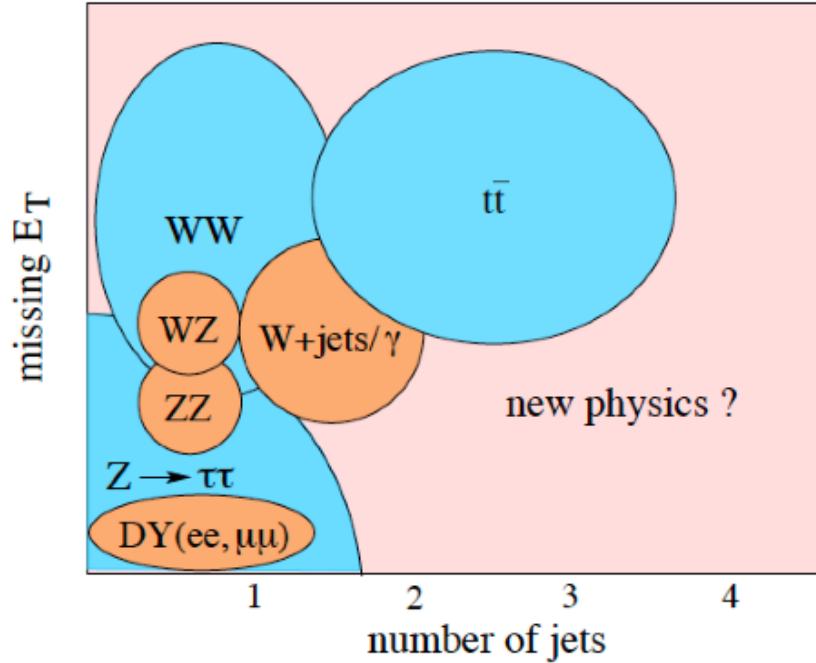


Figure 16: Schematic of expected placement of contributions from our main processes in (N_{jets}, \cancel{E}_T) phase space.

In order to meaningfully compare the number of $e\mu$ events contributed from each sample, shown in Table 6, each sample needs to be scaled such that it corresponds to the same luminosity. Theoretical cross-section estimates good to roughly 10% were used [7]. In this analysis, we chose to scaled to the luminosity of the top mixed sample, 98.7 pb^{-1} , and the details for how these scaling factors were calculated are provided in Table 5. The scaling factor is given by the ratio of 98.7

pb^{-1} to the luminosity of the sample in pb^{-1} . The number of $e\mu$ events obtained from each sample scaled to 98.7 pb^{-1} is given in Table 6.

Finally, several events from the top mixed phase space plot were selected by using a ROOT random number generator that is weighted according to the histogram shape, and these can be thought of as representative of the first $e\mu$ events we would expect from real data. The coordinates of these events in the (N_{jets}, \cancel{E}_T) phase space are noted in Tables 7 - 13, and the relative contributions of the different samples to these bins are calculated. For each of the 7 top mixed events, we can determine an estimate for the probability that the event came from a $t\bar{t}$, WW , $Z \rightarrow \tau\tau$, or a background process. It is assumed that only the samples used in this analysis contribute. Therefore, when the first real $e\mu$ data events are detected, they can be plotted in this phase space to obtain an idea of what decay produced them.

The $Z \rightarrow \tau\tau$ sample is composed of 6 files corresponding to samples generated separately with 0 to 5 additional partons. Figures 30- 35 show how various kinematic quantities depend on parton number for this process.

Process	MC Sample File Name
Main	
$t\bar{t}$	mc08.105200.T1_McAtNlo_Jimmy.merge.AOD.e357_s462_s520_r809_r838/
$Z \rightarrow \tau\tau$	mc08.10767*.AlpGenJimmyZtautauNp * _pt20.merge.AOD.e376_s462_s520_r808_r838/with* = 0, 1, 2, 3, 4, 5partons
WW	mc08.105985.WW_Herwig.merge.AOD.e379_s462_s520_r808_r838/
Background	
$W + \gamma$	
$W\mu^+\gamma$	mc08.108289.Pythia_MadGraph_Wplusmunugamma.merge.AOD.e452_s495_s520_r808_r838/
$W\mu^-\gamma$	mc08.108289.Pythia_MadGraph_Wminusmunugamma.merge.AOD.e452_s495_s520_r808_r838/
$W + jets$	
$W e\nu$	mc08.10768*.AlpGenJimmyWenuNp * _pt20.merge.AOD.e368_s462_s520_r808_r838/with* = 0 - 5
$W\mu\nu_{mu}$	mc08.10769*.AlpGenJimmyWmunuNp * _pt20.merge.AOD.e368_s462_s520_r808_r838/with * 0 = 5
$W\tau\nu_{tau}$	mc08.10770*.AlpGenJimmyWtaunuNp * _pt20.merge.AOD.e368_s462_s520_r808_r838/with* = 0 - 5
WZ	mc08.105987.WZ_Herwig.merge.AOD.e368_s462_s520_r808_r838/
ZZ	mc08.105986.ZZ_Herwig.merge.AOD.e379_s462_s520_r808_r838/
Top Mixed	user.RichardHawkings.0108177.topmix_Muon.AOD.v6

Table 4: File names of MC samples used. The mc08 files are for 10 TeV collisions. Jet reconstruction AntiKt4H1TopoJets was used.

Process	Number Events: Generated	GenFilter Efficiency	σ_{theory} (pb) $\pm 10\%$	Luminosity: (fb ⁻¹) $\pm 10\%$	Scale Factor $\pm 10\%$
$t\bar{t}$	$4.49 \cdot 10^6$	0.55	414	19.7	0.005
WW	$1.0 \cdot 10^5$	0.3717	74	3.63	0.027
$Z \rightarrow \tau\tau$ 0p	$2.71 \cdot 10^5$	1.0	1,230	0.220	0.329
$Z \rightarrow \tau\tau$ 1p	$6.25 \cdot 10^4$	1.0	286	0.219	0.331
$Z \rightarrow \tau\tau$ 2p	$2.1 \cdot 10^5$	1.0	96	2.30	0.033
$Z \rightarrow \tau\tau$ 3p	$6.35 \cdot 10^4$	1.0	29	2.20	0.033
$Z \rightarrow \tau\tau$ 4p	$1.85 \cdot 10^4$	1.0	8.2	2.26	0.032
$Z \rightarrow \tau\tau$ 5p	$5.5 \cdot 10^3$	1.0	2.3	2.37	0.031
$W\mu^+\gamma$	50,000	1.0	292	0.171	0.576
$W\mu^-\gamma$	50,000	1.0	292	0.171	0.576
WZ	328,455	1.0	32	10.3	0.001
ZZ	532,777	1.0	10.5	50.7	0.002
$W e \nu_e$ 0p	2,957,500	1.0	13,300	0.222	0.445
$W e \nu_e$ 1p	637,500	1.0	2770	0.231	0.428
$W e \nu_e$ 2p	2,030,500	1.0	885	2.29	0.043
$W e \nu_e$ 3p	608,000	1.0	266	2.28	0.043
$W e \nu_e$ 4p	167,000	1.0	73	2.27	0.043
$W e \nu_e$ 5p	50,000	1.0	22	2.30	0.043
$W \mu \nu_\mu$ 0p	3,048,000	1.0	13,300	0.229	0.432
$W \mu \nu_\mu$ 1p	623,000	1.0	2,840	0.219	0.450
$W \mu \nu_\mu$ 2p	2,031,000	1.0	898	2.261	0.044
$W \mu \nu_\mu$ 3p	607,500	1.0	266	2.284	0.043
$W \mu \nu_\mu$ 4p	167,000	1.0	73	2.285	0.043
$W \mu \nu_\mu$ 5p	50,000	1.0	21	2.330	0.042
$W \tau \nu_\tau$ 0p	3,049,000	1.0	13,300	0.229	0.432
$W \tau \nu_\tau$ 1p	621,000	1.0	2760	0.225	0.439
$W \tau \nu_\tau$ 2p	2,030,000	1.0	881	2.30	0.043
$W \tau \nu_\tau$ 3p	607,500	1.0	266	2.29	0.043
$W \tau \nu_\tau$ 4p	166,500	1.0	72	2.30	0.043
$W \tau \nu_\tau$ 5p	50,000	1.0	22	2.25	0.044

Table 5: Scaling factor calculation.

Process	Total Number of Events for 98.7 pb ⁻¹ of Data: ±10%	Number of $e\mu$ Events
Top Mixed Sample	1, 170, 000 ± 100, 000	1900 ± 200
$t\bar{t}$	11, 350 ± 1, 130	329 ± 32
WW	1360 ± 140	41.8 ± 4.3
$Z \rightarrow \tau\tau$ Total Contribution	119, 000 ± 12, 000	248 ± 26
$Z \rightarrow \tau\tau$ 0p	89, 000 ± 9, 000	158 ± 23
$Z \rightarrow \tau\tau$ 1p	20, 500 ± 2, 000	54.5 ± 8.6
$Z \rightarrow \tau\tau$ 2p	6, 940 ± 690	22.8 ± 3.2
$Z \rightarrow \tau\tau$ 3p	2, 080 ± 210	8.43 ± 1.27
$Z \rightarrow \tau\tau$ 4p	592 ± 59	2.82 ± 0.49
$Z \rightarrow \tau\tau$ 5p	167 ± 17	1.28 ± 0.26
WZ	960 ± 100	6.60 ± 0.71
ZZ	97.2 ± 9.7	0.43 ± 0.05
W + jets Total Contribution	1, 560, 000 ± 160, 000	357 ± 35
$W e \nu_e$ Total Contribution	139, 000 ± 14, 000	5.42 ± 0.93
$W \mu \nu_\mu$ Total Contribution	738, 000 ± 74, 000	335 ± 35
$W \tau \nu_\tau$ Total Contribution	684, 000 ± 68, 000	17.1 ± 2.5
$W \mu^\pm \gamma$ Total Contribution	57, 600 ± 5, 800	228 ± 20
Grand Total (excluding Top Mixed Sample)	1, 750, 000 ± 180, 000	1, 210 ± 60

Table 6: Number of $e\mu$ events contributed by each sample.

Bin Coordinates	Coordinates in (N_{jets}, \cancel{E}_T) Phase Space
(3,14)	(2,270 GeV)
Process	# Events from Process / Total in Bin
$t\bar{t}$	0.712716
WW	0
$Z \rightarrow \tau\tau$ Total Contribution	0
$W e \nu_e$ Total Contribution	0
$W \mu \nu_\mu$ Total Contribution	0.287284
$W \tau \nu_\tau$ Total Contribution	0
WZ	0
ZZ	0
$W \mu^\pm \gamma$ Total Contribution	0

Table 7: Composition of bins for randomly selected “Event 1” by weighting of Top Mixing Sample N_{jets} vs \cancel{E}_T phase space histogram.

Bin Coordinates	Coordinates in (N_{jets}, \cancel{E}_T) Phase Space
(1,2)	(0,30 GeV)
Process	# Events from Process / Total in Bin
$t\bar{t}$	0.049163
WW	0.0387636
$Z \rightarrow \tau\tau$ Total Contribution	0.119281
$W e \nu_e$ Total Contribution	0.00521064
$W \mu \nu_\mu$ Total Contribution	0.361858
$W \tau \nu_\tau$ Total Contribution	0.022632
WZ	0.00484593
ZZ	0.000181532
$W \mu^\pm \gamma$ Total Contribution	0.398064

Table 8: Composition of bins for randomly selected “Event 2” by weighting of Top Mixing Sample N_{jets} vs \cancel{E}_T phase space histogram.

Bin Coordinates	Coordinates in (N_{jets}, \cancel{E}_T) Phase Space
(3,1)	(2,10 GeV)
Process	# Events from Process / Total in Bin
$t\bar{t}$	0.426
WW	0.018
$Z \rightarrow \tau\tau$ Total Contribution	0.258
$W e \nu_e$ Total Contribution	0.005
$W \mu \nu_\mu$ Total Contribution	0.199
$W \tau \nu_\tau$ Total Contribution	0.015
WZ	0.008
ZZ	0.002
$W \mu^\pm \gamma$ Total Contribution	0.069

Table 9: Composition of bins for randomly selected “Event 3” by weighting of Top Mixing Sample N_{jets} vs \cancel{E}_T phase space histogram.

Bin Coordinates	Coordinates in (N_{jets}, \cancel{E}_T) Phase Space
(1,7)	(0,130 GeV)
Process	# Events from Process / Total in Bin
$t\bar{t}$	0.555
WW	0.028
$Z \rightarrow \tau\tau$ Total Contribution	0.046
$W e \nu_e$ Total Contribution	0
$W \mu \nu_\mu$ Total Contribution	0.351
$W \tau \nu_\tau$ Total Contribution	0.017
WZ	0.002
ZZ	0.001
$W \mu^\pm \gamma$ Total Contribution	0

Table 10: Composition of bins for randomly selected “Event 4” by weighting of Top Mixing Sample N_{jets} vs \cancel{E}_T phase space histogram.

Bin Coordinates	Coordinates in (N_{jets}, \cancel{E}_T) Phase Space
(1,3)	(0,50 GeV)
Process	# Events from Process / Total in Bin
$t\bar{t}$	0.099
WW	0.064
$Z \rightarrow \tau\tau$ Total Contribution	0.022
$W e \nu_e$ Total Contribution	0.007
$W \mu \nu_\mu$ Total Contribution	0.429
$W \tau \nu_\tau$ Total Contribution	0.015
WZ	0.010
ZZ	0.000
$W \mu^\pm \gamma$ Total Contribution	0.354

Table 11: Composition of bins for randomly selected “Event 5” by weighting of Top Mixing Sample N_{jets} vs \cancel{E}_T phase space histogram.

Bin Coordinates	Coordinates in (N_{jets}, \cancel{E}_T) Phase Space
(2,4)	(1,70 GeV)
Process	# Events from Process / Total in Bin
$t\bar{t}$	0.550
WW	0.042
$Z \rightarrow \tau\tau$ Total Contribution	0.035
$W e \nu_e$ Total Contribution	0.004
$W \mu \nu_\mu$ Total Contribution	0.271
$W \tau \nu_\tau$ Total Contribution	0.021
WZ	0.006
ZZ	0.000
$W \mu^\pm \gamma$ Total Contribution	0.071

Table 12: Composition of bins for randomly selected “Event 6” by weighting of Top Mixing Sample N_{jets} vs \cancel{E}_T phase space histogram.

Bin Coordinates	Coordinates in (N_{jets}, \cancel{E}_T) Phase Space
(4,2)	(3,30 GeV)
Process	# Events from Process / Total in Bin
$t\bar{t}$	0.774
WW	0.008
$Z \rightarrow \tau\tau$ Total Contribution	0.063
$W e \nu_e$ Total Contribution	0.004
$W \mu \nu_\mu$ Total Contribution	0.143
$W \tau \nu_\tau$ Total Contribution	0.004
WZ	0.004
ZZ	0.001
$W \mu^\pm \gamma$ Total Contribution	0

Table 13: Composition of bins for randomly selected “Event 7” by weighting of Top Mixing Sample N_{jets} vs \cancel{E}_T phase space histogram.

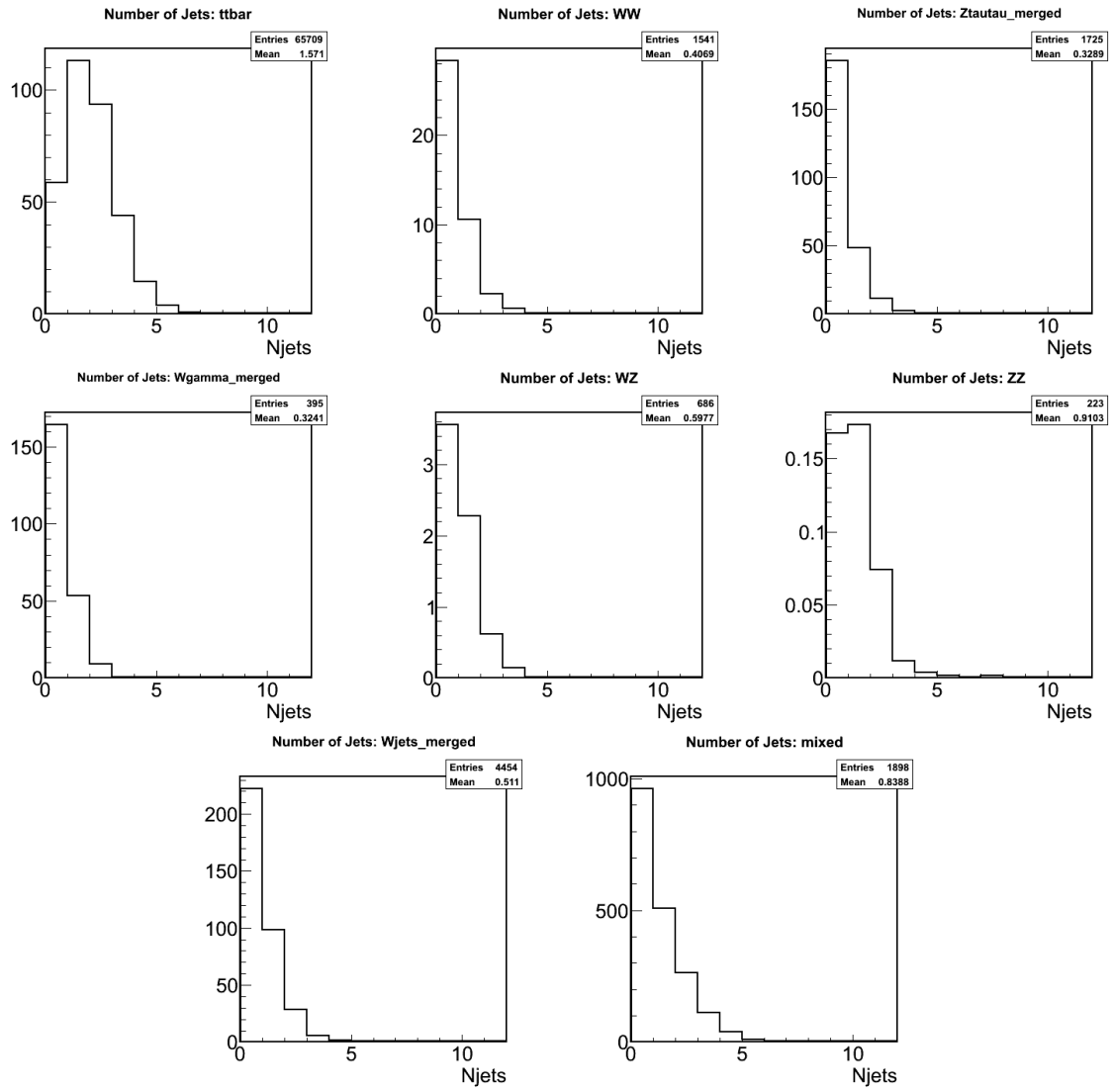


Figure 17: Number of jets for $e\mu$ events.

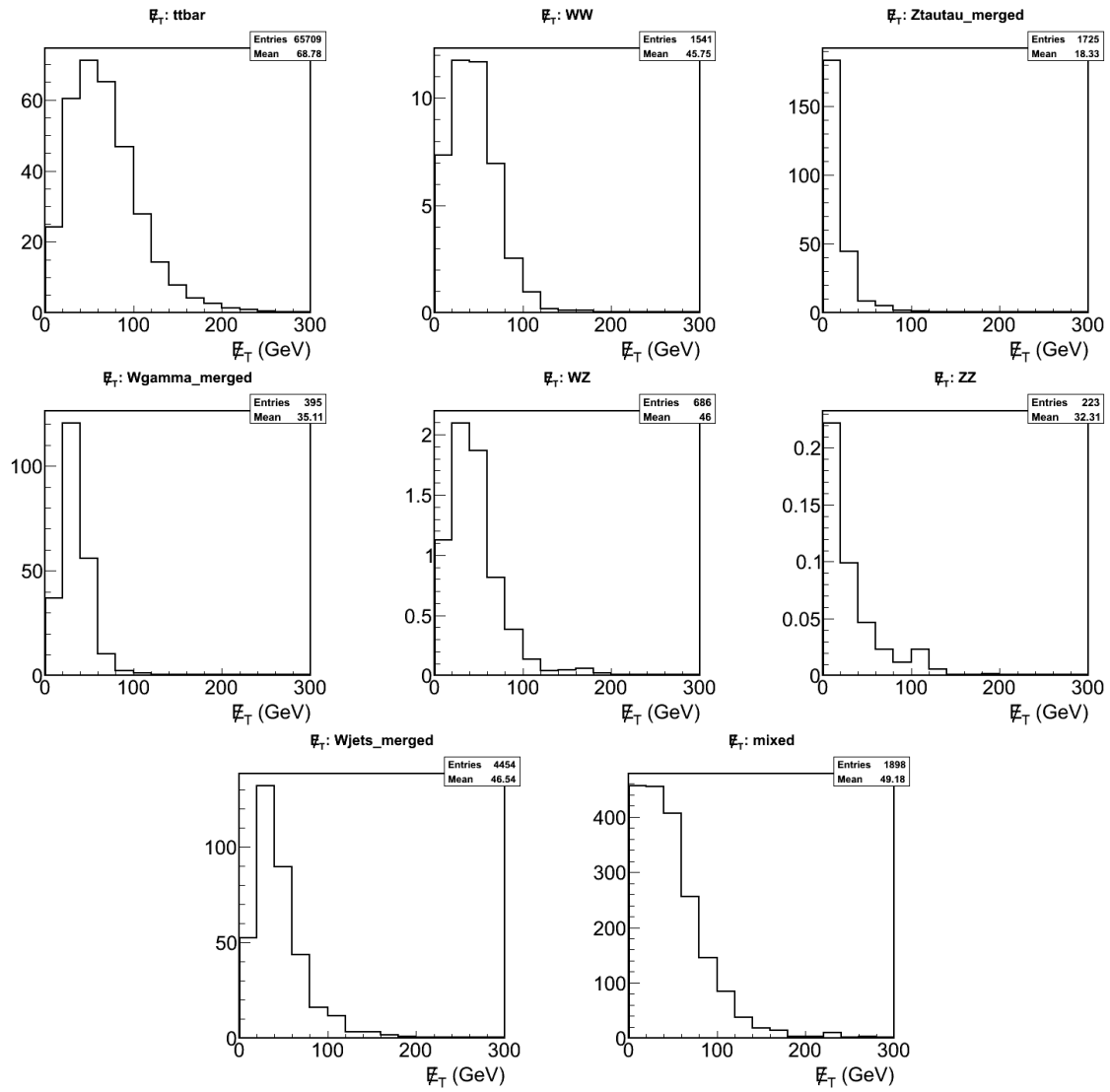


Figure 18: \cancel{E}_T for $e\mu$ events.

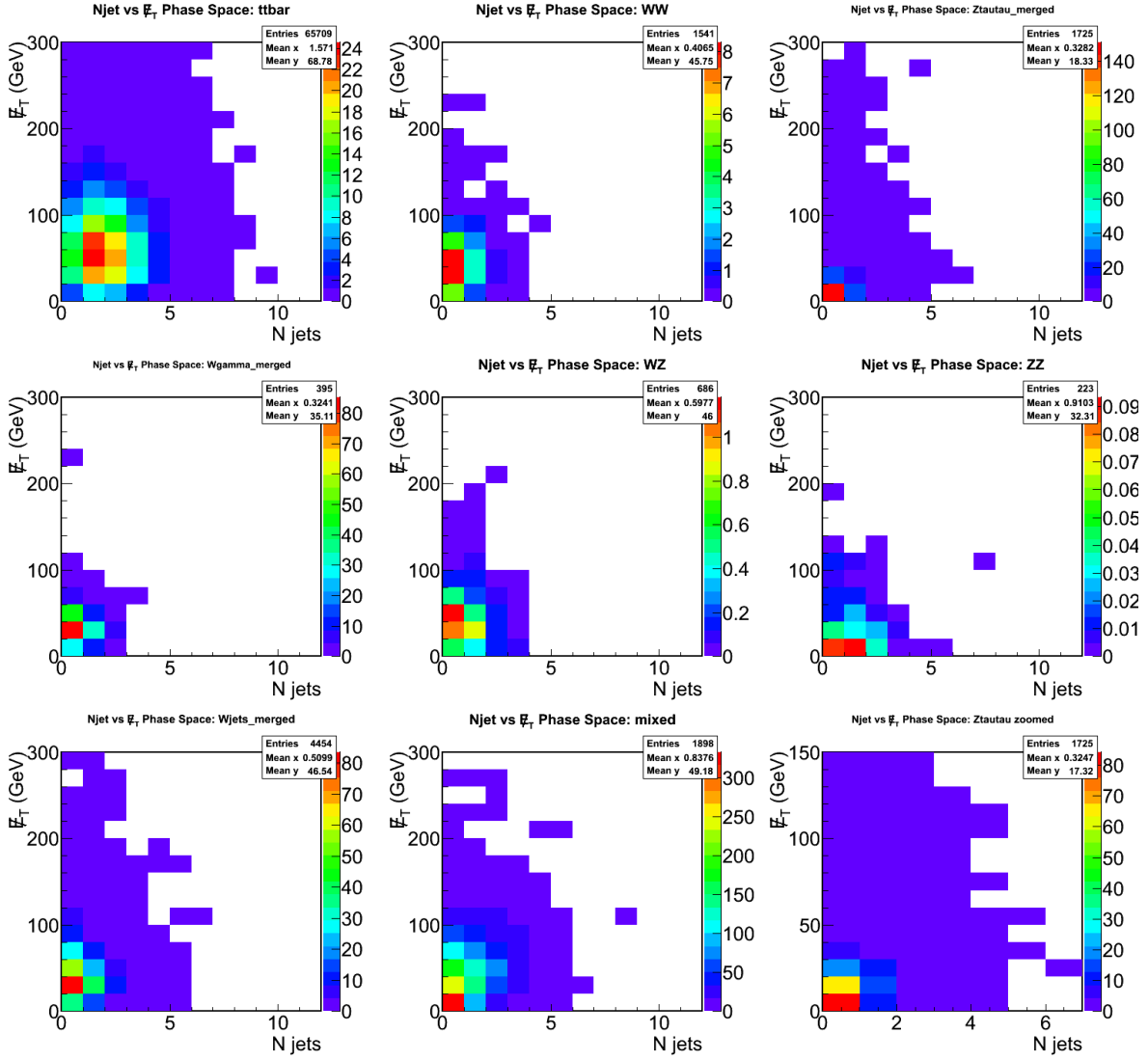


Figure 19: Number of jets versus E_T for $e\mu$ events.

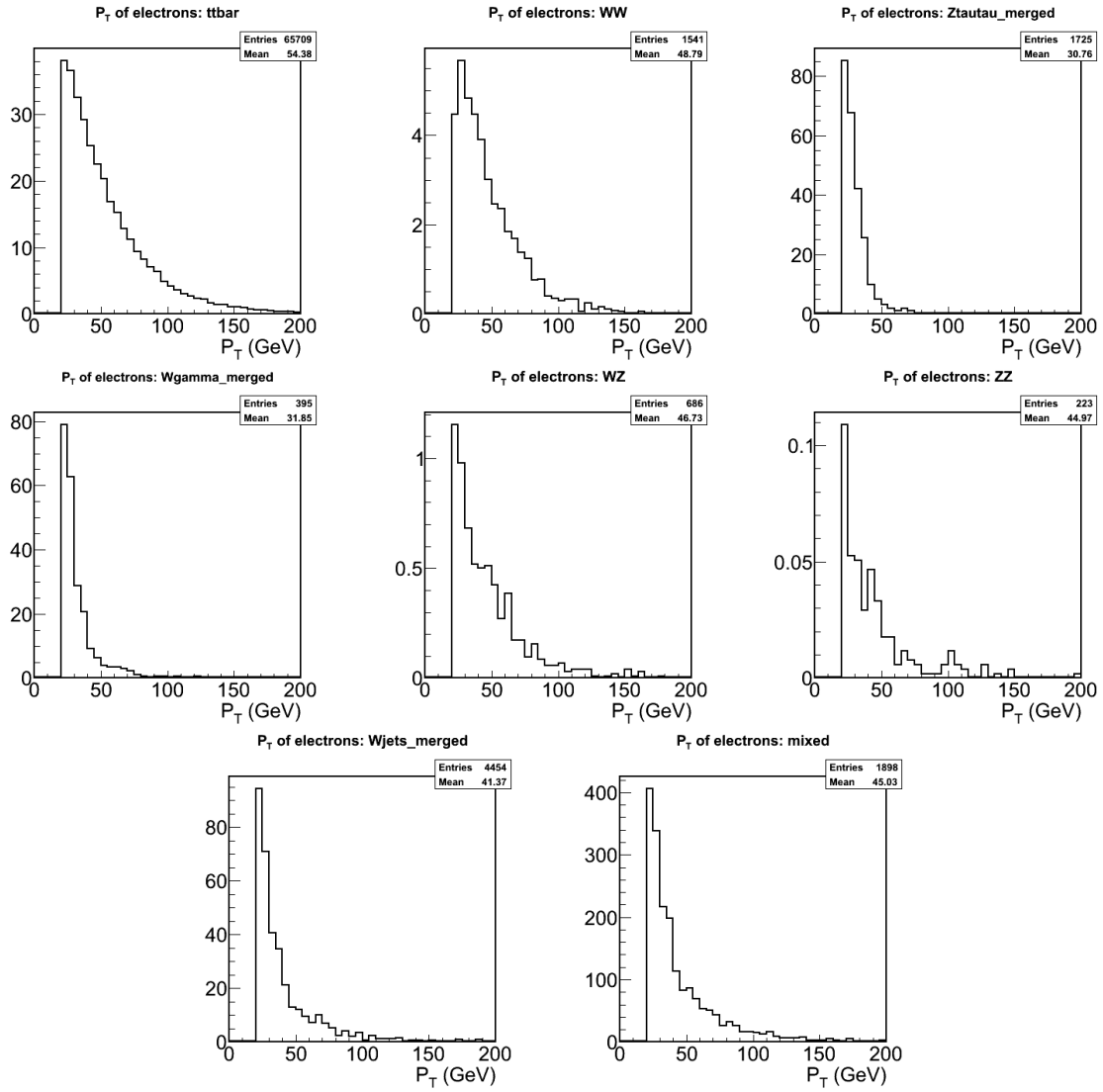


Figure 20: P_T of electrons for $e\mu$ events.

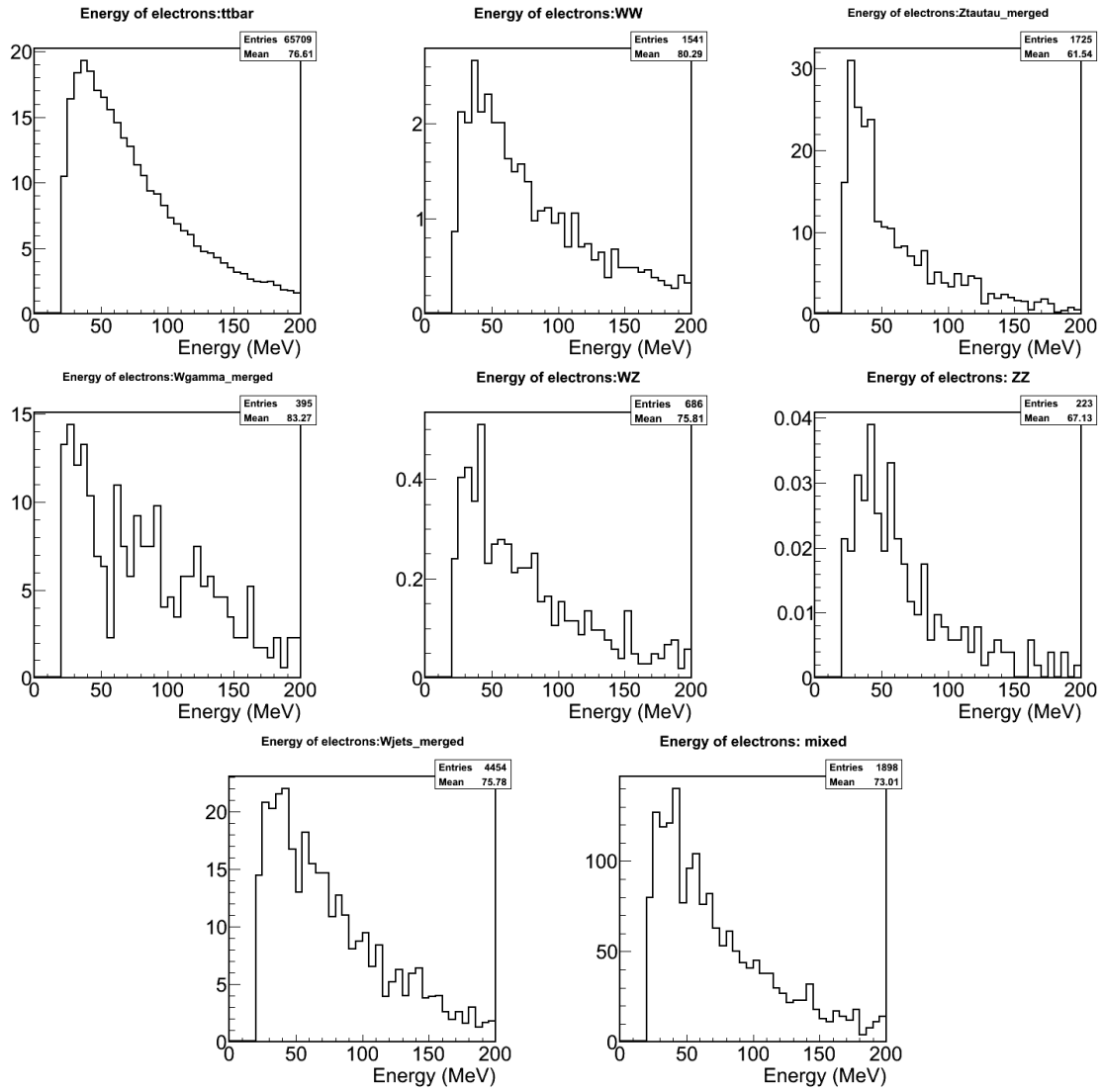


Figure 21: Energy of electrons for $e\mu$ events.

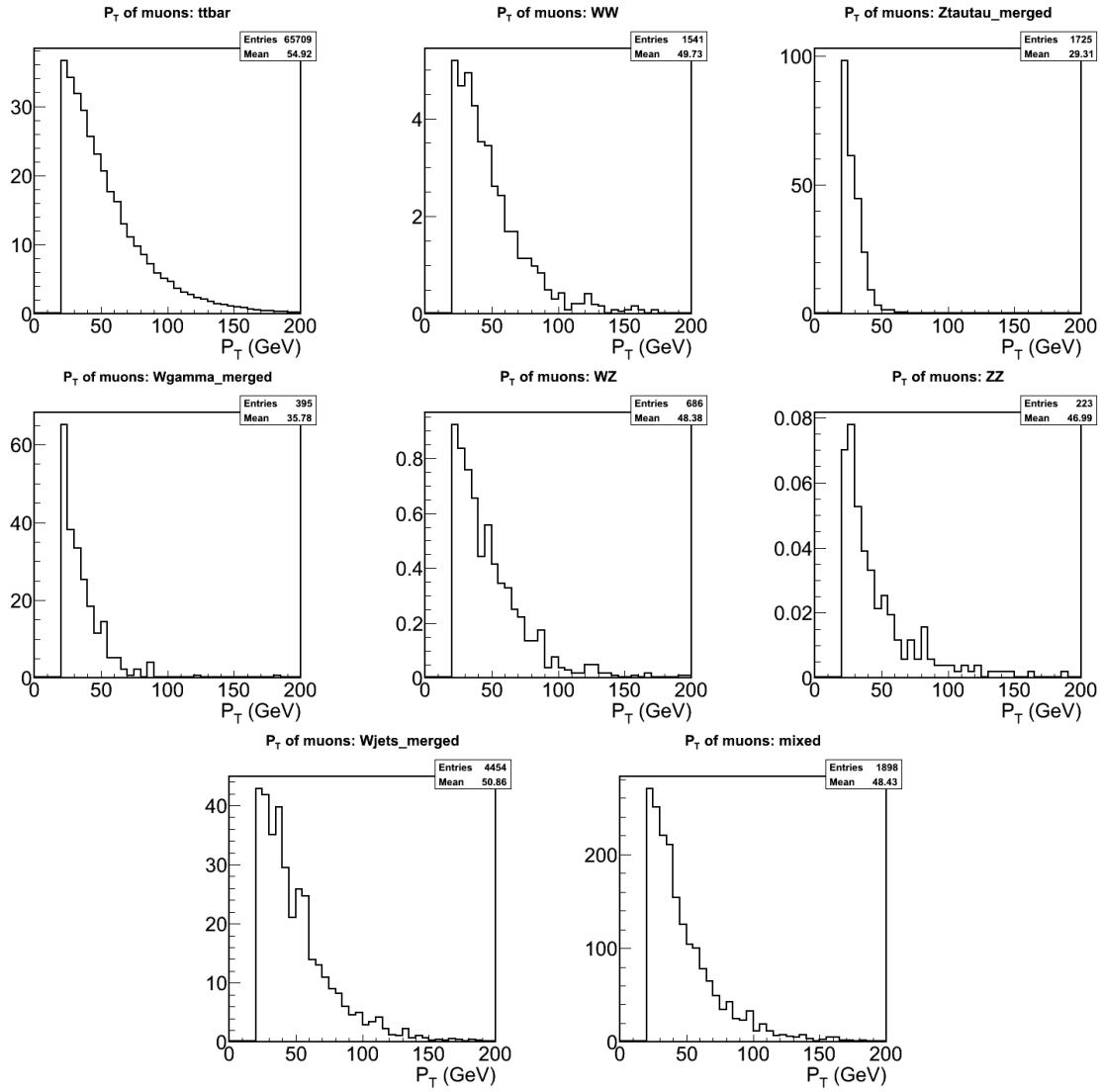


Figure 22: P_T of muons for $e\mu$ events.

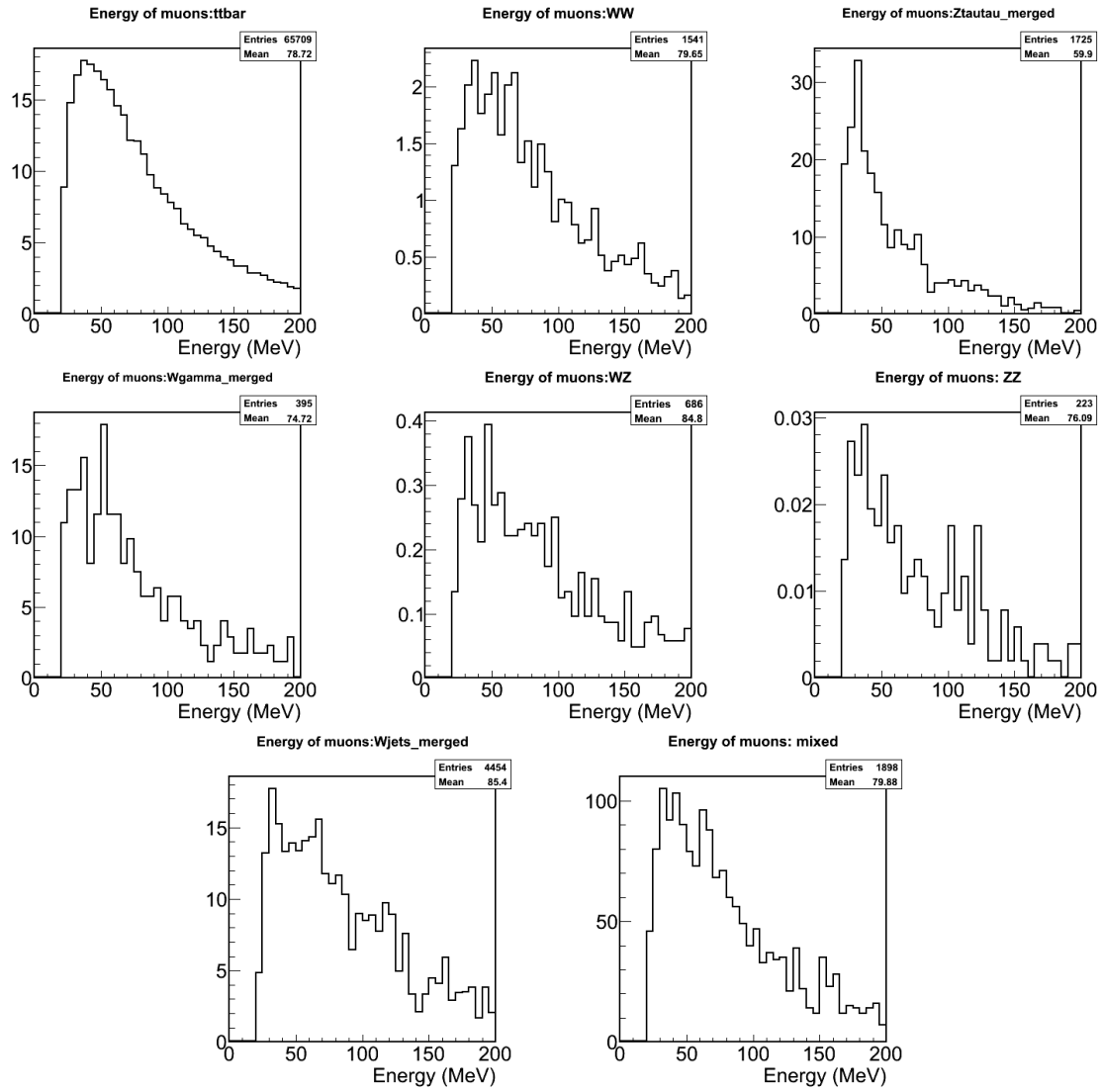


Figure 23: Energy of muons for $e\mu$ events.

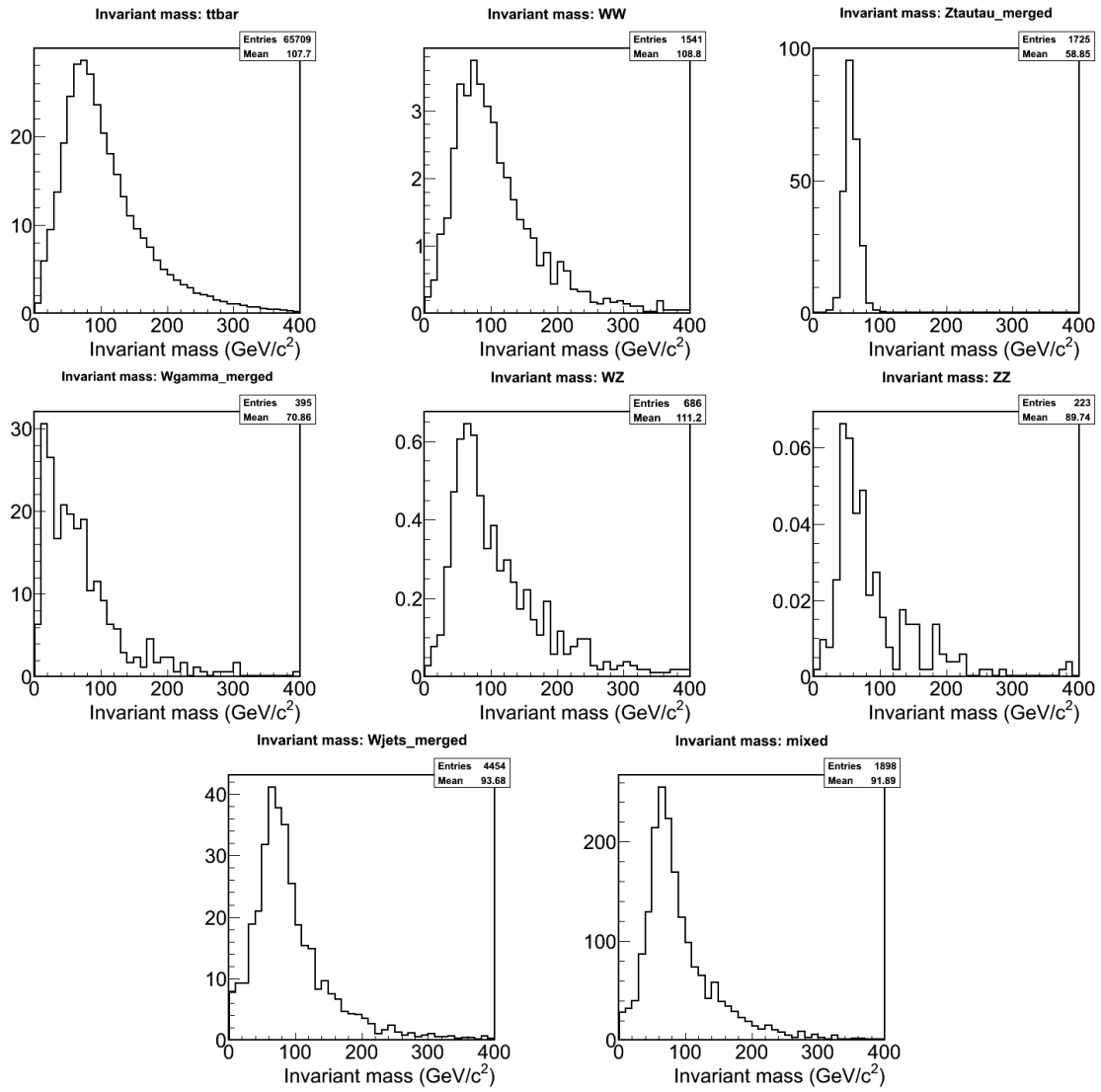


Figure 24: Invariant mass of the two leptons for $e\mu$ events.

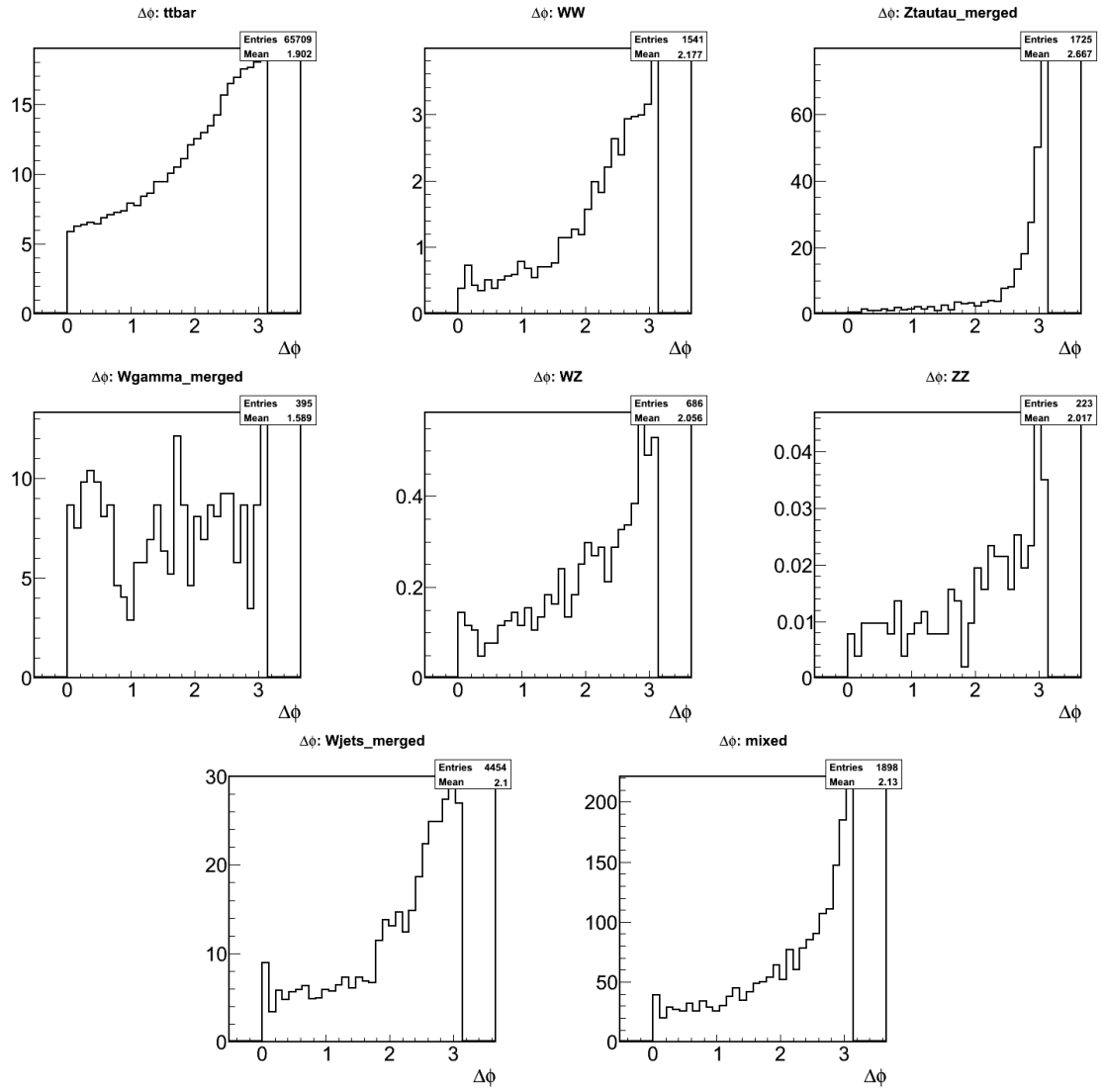


Figure 25: $\Delta\phi$ between electrons and muons for $e\mu$ events.

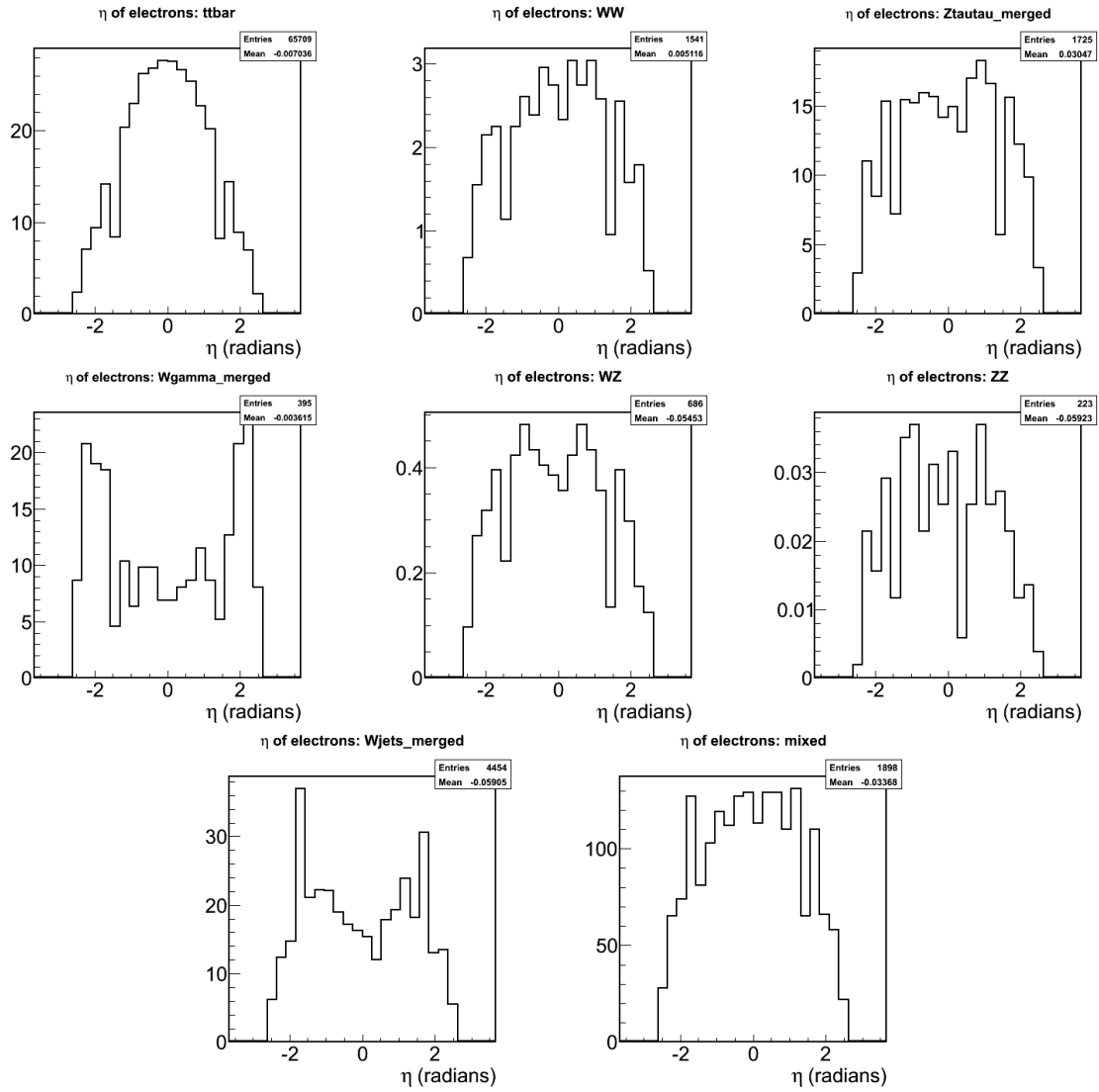


Figure 26: η of electrons for $e\mu$ events.

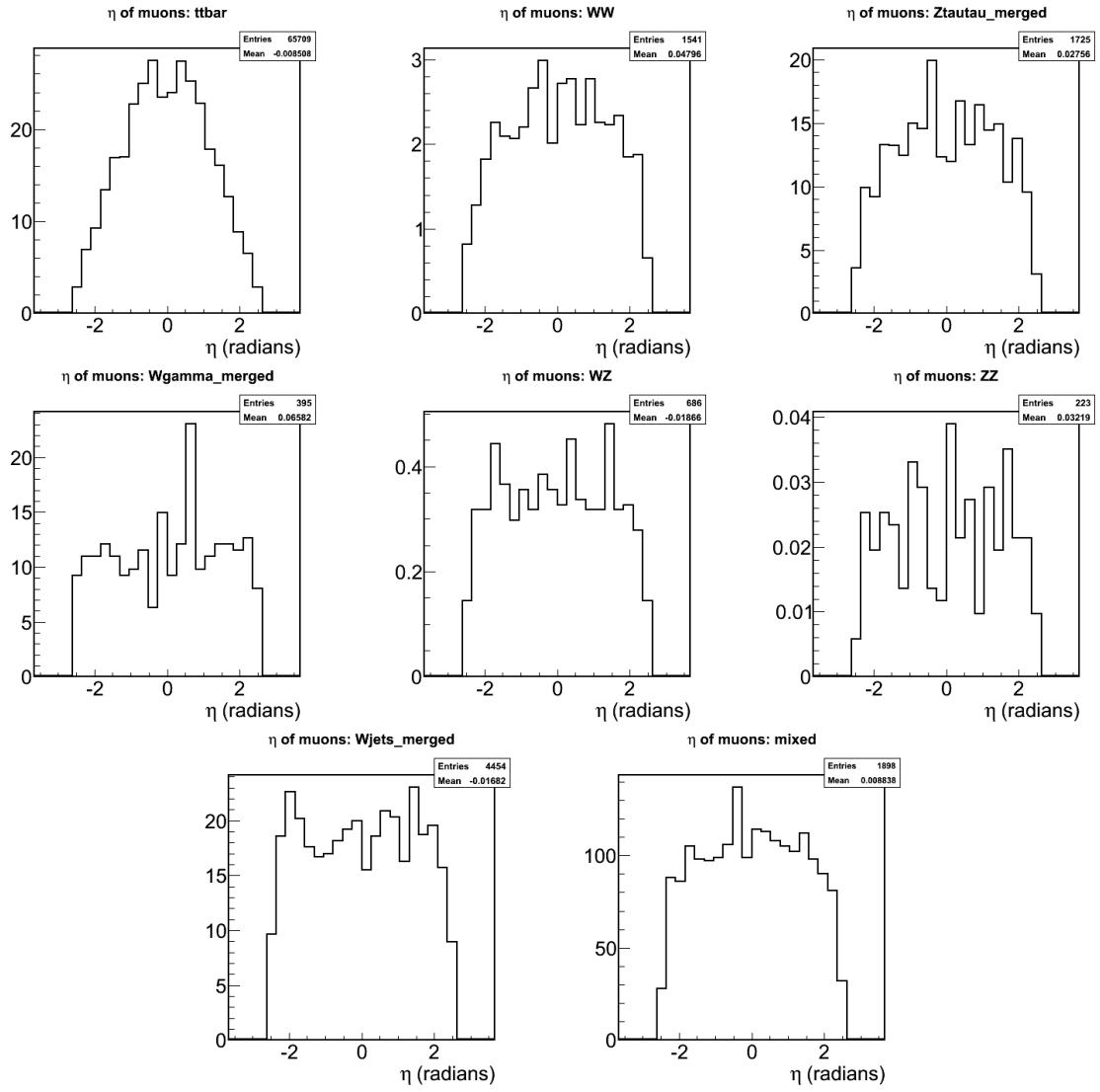


Figure 27: η of muons for $e\mu$ events.

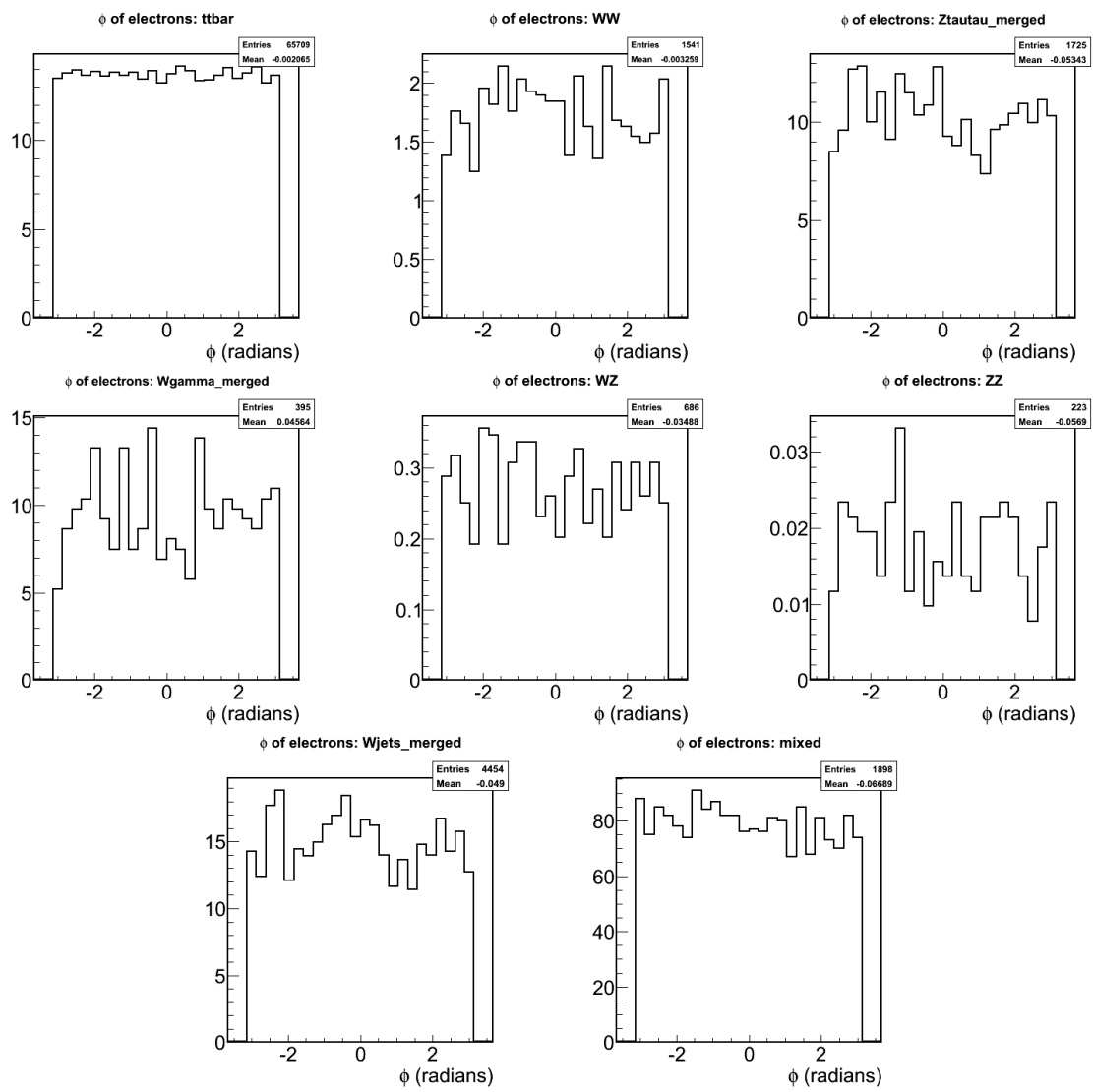


Figure 28: ϕ of electrons for $e\mu$ events.

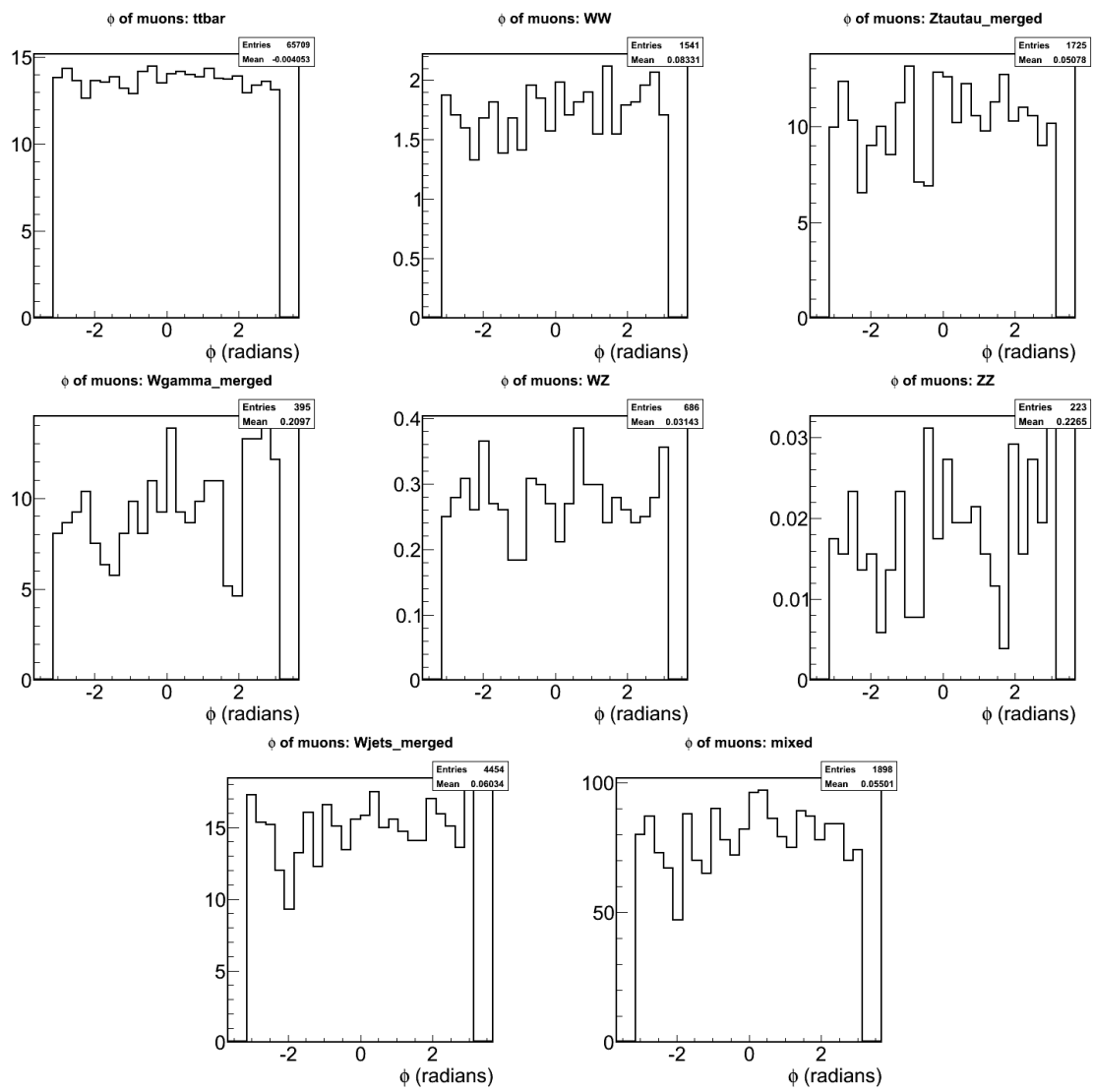


Figure 29: ϕ of muons for $e\mu$ events.

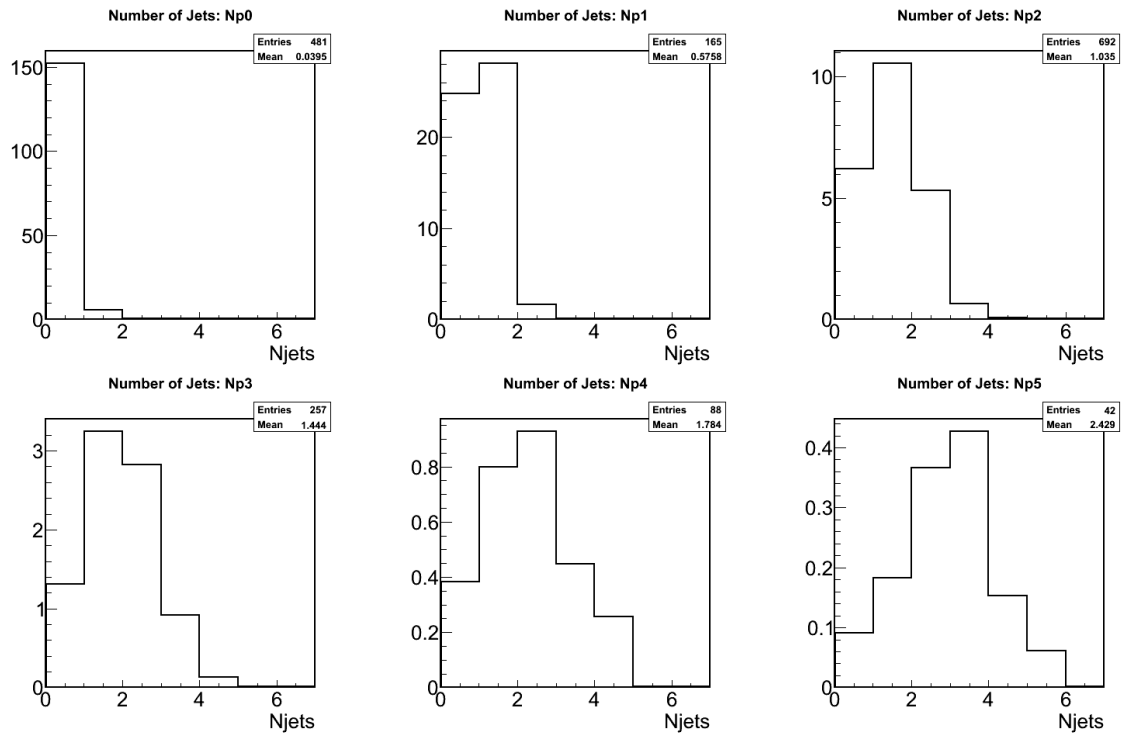


Figure 30: Number of jets for $e\mu$ events. Each parton contribution to the Ztautau sample has been plotted separately.

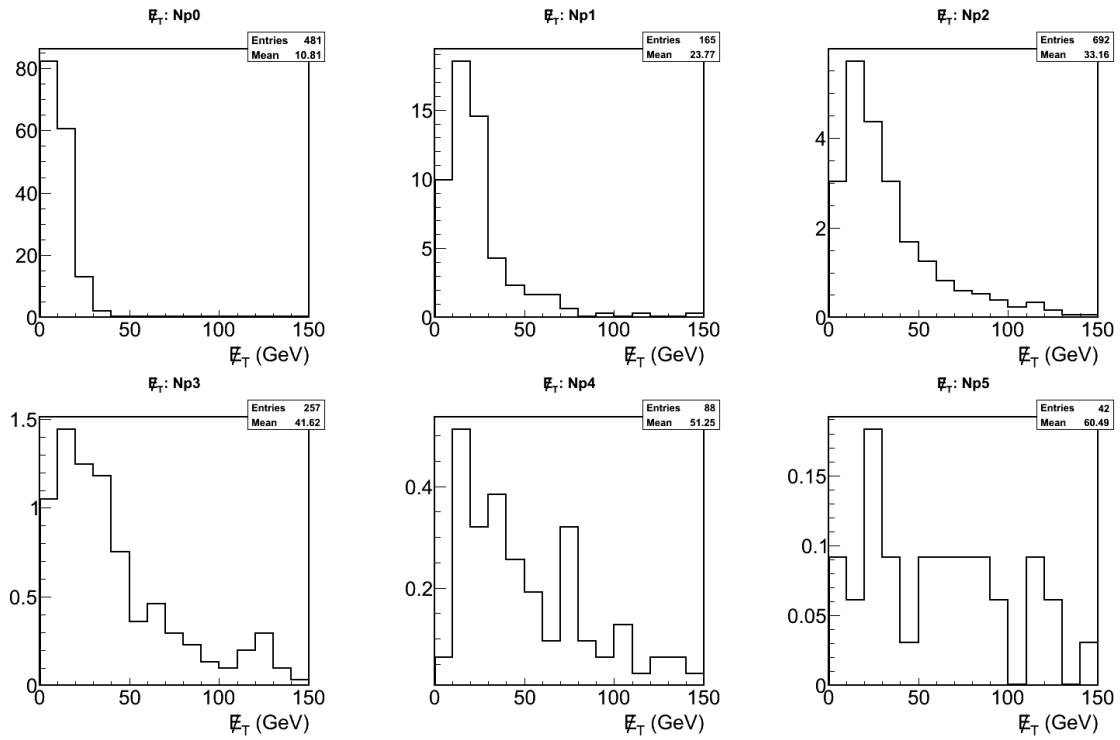


Figure 31: \cancel{E}_T for $e\mu$ events. Each parton contribution to the Ztautau sample has been plotted separately.

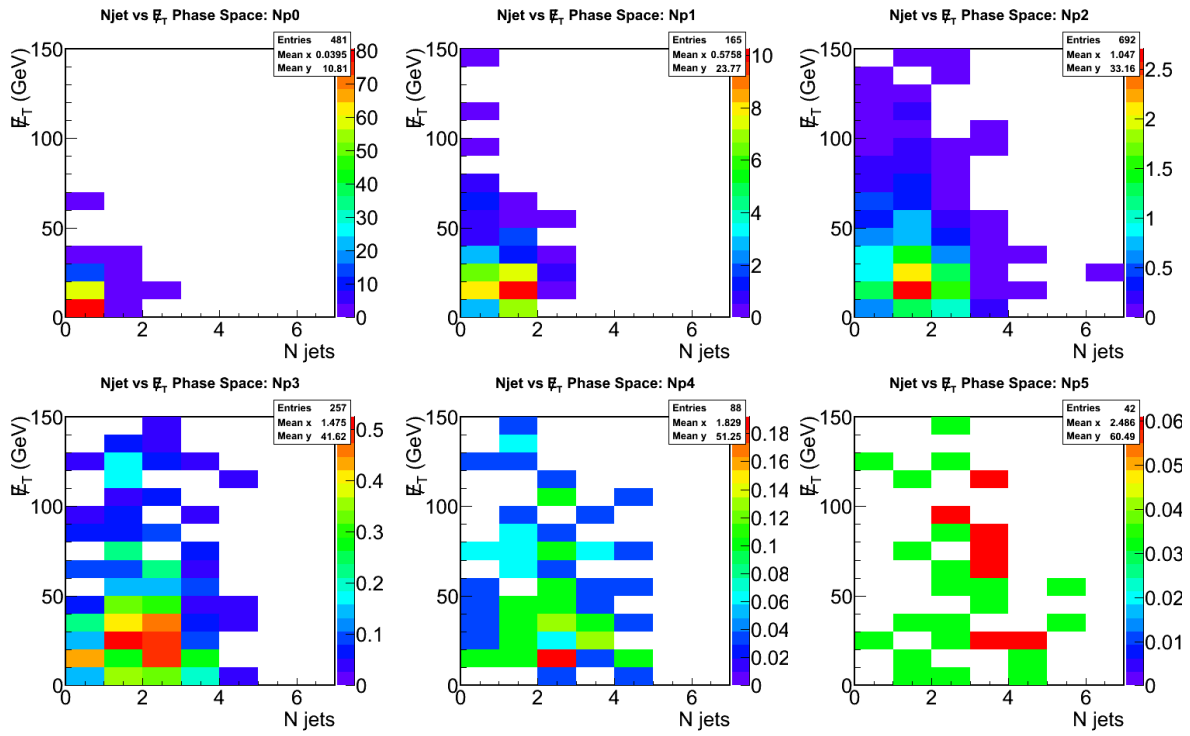


Figure 32: Number of jets versus \cancel{E}_T for $e\mu$ events. Each parton contribution to the $Z\tau\tau$ sample has been plotted separately.

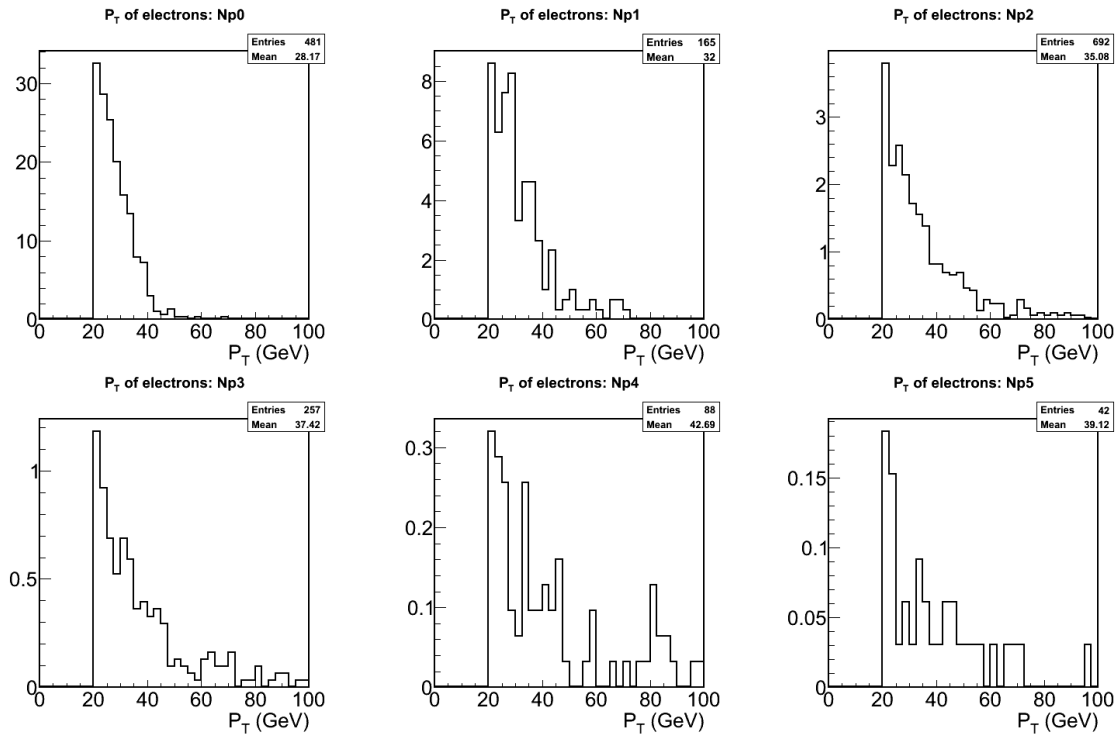


Figure 33: P_T of electrons for $e\mu$ events. Each parton contribution to the Ztautau sample has been plotted separately.

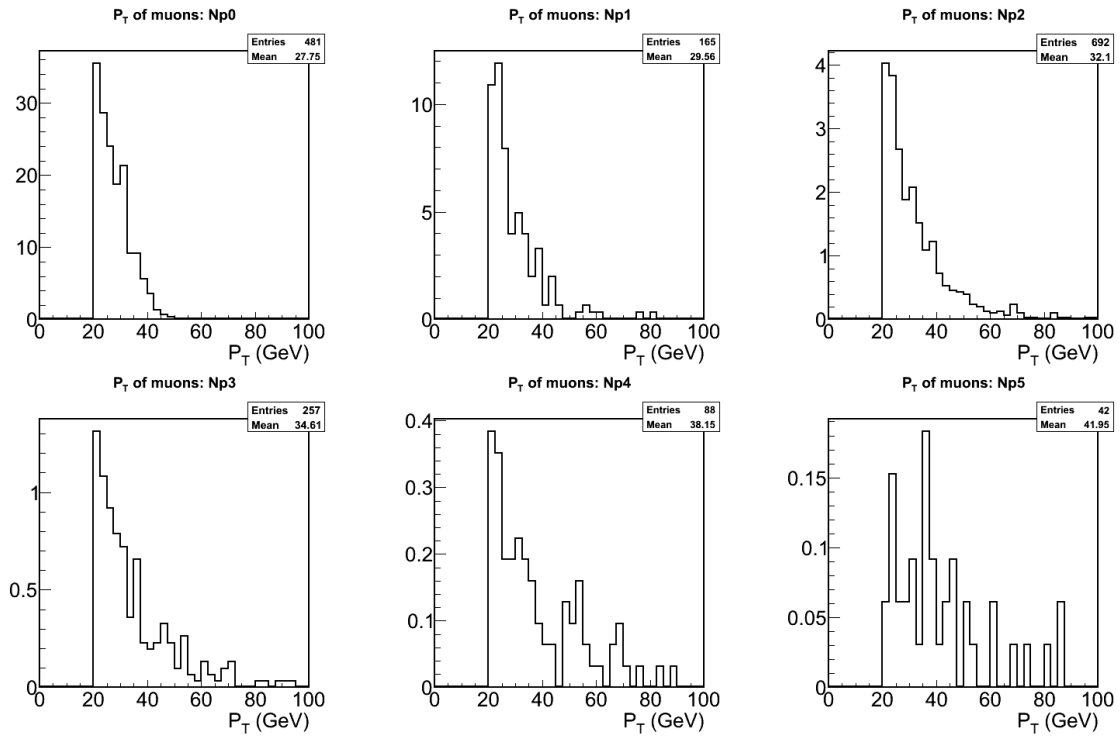


Figure 34: P_T of muons for $e\mu$ events. Each parton contribution to the Ztautau sample has been plotted separately.

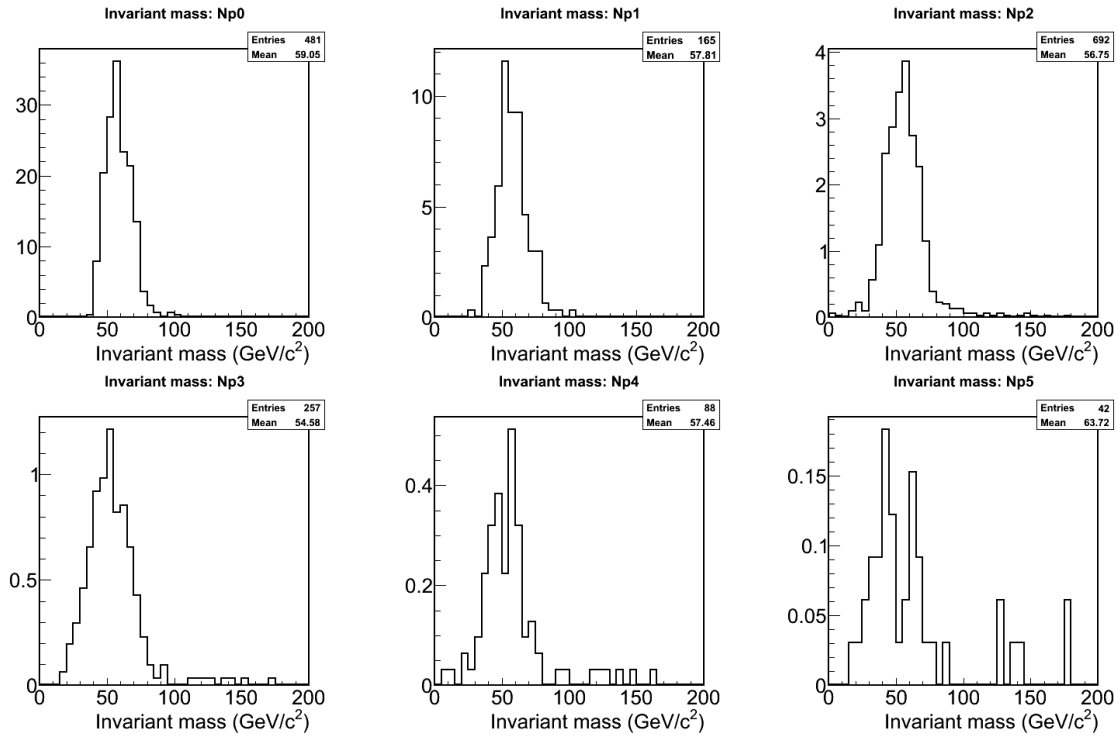


Figure 35: Invariant mass of the two leptons for $e\mu$ events. Each parton contribution to the Ztautau sample has been plotted separately.

6 Conclusion

This study forms the foundation for analyzing the high- p_T dilepton sample. Events with an electron and a muon of opposite charge in the final state are predicted to be rare by the Standard Model. Ultimately, this analysis will be developed to simultaneously extract the cross-sections of our three signal events using the 2-D histograms of $e\mu$ events in the phase space of (N_{jets}, \cancel{E}_T) . By comparing these measurements to the theoretical values for the cross-sections, we can test the Standard Model. Furthermore, these events can be used as tools to search for new physics.

In this study, we have examined how the various processes contribute to the $e\mu$ sample and begun to assess the nature of the contamination by the different background samples and how to reduce them. By studying the various kinematic quantities, we have furthered our understanding of these events, which is an important first step in developing the Global Dilepton analysis framework. Finally, by comparing the relative contributions of the processes to the $e\mu$ sample, we can make a quantitative prediction as to what kind of decay produced a data event given its coordinate in the (N_{jets}, \cancel{E}_T) phase space.

In addition to building a foundation for the Global Dilepton analysis, we also study an unexpected correlation found in both cosmic data and ATLAS Monte Carlo between two quantities relevant to the TRT. We assess whether or not this correlation can be used to determine the mean interaction length in the TRT straw and find this not to be possible given our current technique. However, this study is useful in so far that it prompts us to better understand better both the ATLAS simulation and charge collection mechanism in the TRT, which can ultimately improve tracking resolution at ATLAS.

References

- [1] David Griffiths. *Introduction to Elementary Particles*. Second, Revised Edition. Wiley-VCH, 2009.
- [2] <http://public.web.cern.ch/public/>
- [3] <http://www.atlas.ch>
- [4] http://www.atlas.ch/etours_exper/
- [5] ATLAS CSC Note. The ATLAS Collaboration. "Diboson Physics Studies With the ATLAS Detector," ATL-PHYS-PUB-2008-xxx, 24 March, (2008).
- [6] "Choice of Jet Algorithms in ATLAS" Presentation by ATLAS Collaboration Member Kerstin Perez. http://www.ccsem.infn.it/issp2009/newtalents/KPerez_Erice_JetAlgs_20090905.pdf
- [7] <http://www.ge.infn.it/tosi/cms/topMC.html#crosssections>
- [8] "W mass measurement and simulation of the transition radiation tracker at the ATLAS experiment." Esben Bryndt Klinkby, (Copenhagen U.) . CERN-THESIS-2008-071, Apr 2008. 224pp.